Links between Surface Changes with Strain whitening, Shear Banding and Damage in a Toughened Epoxy Adhesive

Luis F. Trimiño, Duane S. Cronin*

***Department of Mechanical and Mechatronics Engineering**
University of Waterloo, 200 University Avenue West, Waterloo, ON N2L 3G1
ltrimino@uwaterloo.ca, dscronin@uwaterloo.ca

ABSTRACT
Owing to the increased use of toughened epoxy adhesives in current transportation light weighting efforts, it is critical that the damage mechanisms observable as strain whitening in these materials are understood and quantified. Quantification of damage is needed for finite element constitutive models used in structural design; however, thin bond lines in adhesive joints limit direct observation of the adhesive. In this study, microscope observations of bulk material specimens subjected to tensile loading were linked to strain whitening and damage in a toughened epoxy adhesive. Cracks on the surface were observed to open during loading, with strain whitening at the crack tips and with the initiation and propagation of shear bands. The stresses approximated at the crack tips suggested that particle cavitation could be occurring in these regions. Image analysis showed that strain whitening was present at crack tips and that these areas served to initiate the shear-bands.
Changes in tensile specimen stiffness and strength were evaluated during load-unload and reload testing, and were linked to the presence of crack growth, as well as the formation of shear bands. Considering changes in strength, the predicted damage level before failure (D~18%) was lower than that predicted using traditional load-unload stiffness (D~35%), attributed to short-term viscoelastic effects; however, damage calculated from load-reload material stiffness (D~19%) was in good agreement with the damage estimated from changes in strength. A new approach, calculating damage from direct image analysis of strain whitening on the free surface (D~21%) was in good agreement with damage quantified by changes in strength and stiffness, with the benefit of quantifying damage over the loading history of the test sample and identifying areas of damage localization.

Keywords: **Structural epoxy adhesives, Cavitation, Crack Opening, Strain Whitening,, Shear banding, Damage measurements.**

1. INTRODUCTION

The use of modern structural adhesives makes it possible to join dissimilar materials when traditional joining methods (e.g. welding) may not be feasible or when the potential for galvanic corrosion exist (e.g., steel to aluminum). Also the use of adhesives allows for continuous joints with benefits [1–5] relative to traditional discontinuous mechanical joints (bolts, rivets, spot-welds, etc.) because they result in structures that are stiffer, can absorb more energy under extreme deformation, and also reduce unwanted vibrations and stress concentrations at joints [5,6]. Due to the relevance of toughened structural adhesives in current light weighting efforts, it is critical that designers and engineers understand the mechanisms that lead to their failure so that these materials can be used effectively and in accordance with the expected loading demands associated with the intended use of the bonded structure.

Although it is important to acknowledge the potential differences between thin bonds and bulk adhesive materials [7], recent investigations in regards to identification of material properties in epoxy adhesives tend to favor the use of bulk samples. Previous studies by different authors using bonded joints have reported that stress concentrations caused by geometry (fillets) [8,9], complex states of stress (i.e. triaxiality) associated with adhesive thickness [10,11], strain rate effects [12–14], and agglomeration of particles in thin bonds [15], can influence the development of different failure mechanisms in adhesive systems. On the other hand, the use of bulk samples is amenable to the implementation of different experimental techniques that can directly identify the stress-strain response (e.g. Hopkinson bar [16,17], optical techniques [18], grid methods [19,20]) or other parameter of interest such as microhardness [21,22] or fracture toughness [17]). Some of these techniques cannot be implemented otherwise due to the impracticality and constrains imposed by thin bond lines (complex states of stress, stress concentrators, clearance and geometric constrains, etc.). However, the use of bulk samples is limited by the difficulty to obtain pore-free samples [23]. Nevertheless, the use of bulk samples provide results that are independent of the tested geometry, the adherent properties, and avoid the use of reverse identification procedures [23].

A common observation in toughened polymeric materials under tensile loading is the development of strain whitening. Strain whitening then, can be considered as a manifestation of the damage mechanisms that are active in a polymeric material. Although strain whitening is generally associated with crazing [24,25], other phenomena such as cracks, particle debonding and cavitation [26,27] , and shear banding can cause light scattering and manifest as strain whitening.

Structural adhesives can have many different formulations (urea, melamine, epoxy, toughened epoxy with rubber particles, toughened epoxy with hard particles, etc.) [28] which explains the rich mechanical responses that can be observed in these materials when subjected to load (e.g. high elasticity modulus with brittle failure, ductile response with large deformation, differences in fracture toughness) [29–31]. In previous studies [22,32] three different adhesive formulations (a one part epoxy, a two part toughened epoxy, and a one part toughened epoxy) were tested under load. However, the two-part phenol resin epoxy with a thermoplastic phase and silicone content for toughening (DP-460NS)

demonstrated unique characteristics in its mechanical response: high stress to failure (~40 MPa), large deformation accompanied with the development of both strain whitening and shear banding. At ultimate failure (e~0.2), the material typically exhibited the characteristics of a brittle fracture at the failure plane. Given these mechanical characteristics and the relevance of toughened adhesives in modern engineering design [5,6,28,33], this adhesive was selected to further investigate the causes of strain whitening and quantification of damage.

Toughened polymeric materials can contain initial defects (e.g., cracks, surface non-uniformities, etc.) which serve as initiation points for the development of damage mechanisms such as crazing, particle cavitation and shear banding. Crazing can be described as the development of fibrils/tendons that delay crack opening and allow the material to absorb more deformation energy prior to ultimate failure. Although crazing is a significant failure mechanism in toughened thermoplastics [9], it is a controversial topic in epoxy materials. While certain authors acknowledge the possibility as presented by Yee and Pearson [34]; others as presented by Garg [29] dispute the presence of this mechanism. To further complicate the subject, craze-like damage in toughened epoxies has been reported in the literature [35,36].

Craze-like damage was explained by Sue [35] as load carrying fibrils or tendons that arrest crack growth initiated from scattered cavitation in the core-shell particles (Butadiene particles surrounded by a hard shell material) used to modify an epoxy matrix. Cavitation in this context (damage in materials), can be understood as the creation and propagation of voids inside a solid due to a hydrostatic, or tri-axial, tensile stress.

Damage due to particle cavitation can also manifest as strain whitening. In this case, the voids created by the cavitation at a particle are responsible for reflecting light and can explain the changes towards a whitened color. The critical stress to initiate void nucleation and cavitation in a particle depend on the initial size, modulus of elasticity and the fracture energy of the embedded particle material [37]. A critical stress value (σ_c) to initiate cavitation can be approximated by the modulus of elasticity (E) for rubber inclusions (Equation 1) ranging from 0.5 μm to 1 mm in diameter [37].

$$E_{d\sim 1mm} \leq \sigma_c \leq 3E_{d\sim 0.5\mu m}$$

Equation 1

The development of plastic zones around crack tips can play a role in energy absorption and delaying failure in polymeric materials [29,38]. Light scattering in crack tips can also contribute to the strain whitening. For microscopic cracks, Gent [39] investigated the expression developed by Inglis [40] (Equation 2) to calculate the stress concentration factor (k) in terms of the crack length (l) and the tip radius (r). Gent explains that the most severe edge flaws which might occur by chance in smooth machined surfaces, would be about 100 μm long and about 10Å in tip radius. This corresponds to a value for k of about 200. However, Gent proposed stress concentration values ranging from 10 to 50 [39] as a

more reasonable figures for edge flaws in normal tensile test-pieces. Patterson proposed a stress concentration factor of 25 [41].

$$k = 1 + 2\sqrt{\frac{l}{r}}$$

Equation 2

Ductile polymers can also deform by developing shear bands[38,42–44]. Shear bands can be identified by areas that are birefringent and are oriented at well-defined angles, typically 45° relative to the axis of principal loading. Shear bands generally initiate at stress concentration points and can develop locally high strains, well above the nominal strain in the material [43,45,46]

The consequence of physical damage to a toughened polymer in the form of cracks, cavitation and shear bands can be described in a quantitative manner using the concept of damage (D). A widely-used definition of damage is a process in which voids and defects grow inside a volume of material until fracture is unavoidable, quantified as the ratio between the volume of voids (V_D) in a representative volume of material (V) (Equation 3). Alternatively, the ratio between the area of voids (A_D) that intersect a plane and area of the plane (A) [47].

$$D = \frac{V_D}{V} \; or \; D = \frac{A_D}{A}$$

Equation 3

According to Lemaitre [47,48], the average damage experienced by a material can be calculated indirectly by using the changes between the material modulus of elasticity (E_o) and the modulus of elasticity during unloading (E**) (Equation 4). Load-unload has been used repeatedly in the literature to measure damage in polymers [17,49–51].

$$\overline{D} = 1 - \frac{E^{**}}{E_o}$$

Equation 4

In addition to changes in modulus of elasticity, variations in effective stress can also be used to determine the amount of damage that a material has sustained. If all defects are open such that there are no forces acting on the surfaces of the defects, then an effective stress ($\bar{\sigma}$) can be related to the ultimate strength of the material (σ) and therefore give a definition of damage (Equation 5) [47].

$$D = 1 - \frac{\bar{\sigma}}{\sigma}$$

Equation 5

Although the literature reports the effects of damage in adhesive joints such as changes in fatigue performance [52,53], crack growth prediction [54], strain fields in patched repairs [55,56], and failure analysis of joints [57]. The material is typically link to specific industry applications (composites and composites repair for aerospace [58–61], wind energy [62], boat construction [63], pipe industry [64]) or with the development of health monitoring techniques for field service assessment [65–68]. However, there is paucity of information regarding quantification of the actual damage that the previously described mechanisms (plastic zones at crack tips, particle cavitation, and shear banding) can introduce in actual structural adhesives. In the present study, damage was assessed using bulk samples made from a structural epoxy adhesive by applying uniaxial tensile deformations, enabling both direct and indirect measures of damage. The bulk specimen surfaces were observed using an opto-digital microscope while under tensile loading to determine the causes for the strain whitening and to evaluate observable damage in the material. Damage from traditional indirect measurements such as changes in modulus and changes in effective stress were used for comparison and to evaluate damage from the optical observation.

2. METHODS

2.1. Material and specimen geometry

A two-part thermoplastic epoxy adhesive (DP-460NS, 3M, Minnesota) toughened with Methyl Methacrylate-Butadiene-Styrene, MBS was used to investigate damage evolution under quasi-static loading. . Epoxy sheets, 3mm in thickness, were manufactured by casting the adhesive material between two glass plates followed by oven curing at the manufacturer specification, i.e. 70°C for two hours [69]. The tensile sample geometry (Figure 1) consisted of a grip zone and a narrow test gauge, 3 mm in width and 12.5 mm in length. The samples were machined from the casted sheets and tested in uniaxial tension. The tested geometry has been used in previous work [22,32] and demonstrate tensile behavior comparable to that of the ASTM type V geometry [32]. Table 1 summarizes typical mechanical properties for this material.

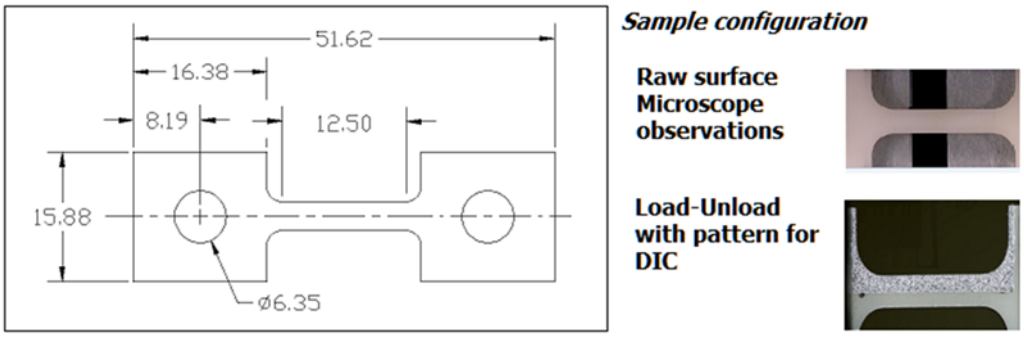

Figure 1: Tensile coupon geometry and configuration for testing

Density [kg/m^3]	Modulus of Elasticity [GPa]	Poisson Ratio ν	Ultimate Stress [MPa] @ 0.002 s^{-1}
1200	2.52±0.34	0.41	39.03±3.56

Table 1: Mechanical properties DP-460NS [22]

2.2. Microscope observations

Two randomly selected specimens were loaded in tension to specific strain levels (Table 2, Figure 2) using a tensile load frame and were observed using an optical digital microscope (ODM) (Keyence VHX-5000, Keyence, Japan). The specimens did not have any previous preparation (Figure 1, top right hand) and the illumination setting was fixed for all observations (~75% brightness). A region of the material with an easily distinguishable feature for identification was selected to enable observations at high magnification (> 500x). The region incorporated the entire width of the specimen in the gauge section (3mm) and a length of 1mm. Although the length of the image was limited by the capacity of the ODM to stitch images, the proposed area was large enough to capture the features evolving on the surface of the material due to the damage processes at the microscopic level. The image length was in agreement with the projection of a representative volumetric element (1 mm^3) that could capture the average damage process in polymeric materials as proposed by Lemaitre [47]. The strain levels selected allowed for observation of the material in four key regions of the strain-stress response: elastic, pre-yield, post-yield, and just prior to ultimate failure (Figure 2, square points). The yield was assumed to correspond with the extrinsic yield point (Figure 2, triangle point), which was determined using *Considères* construction [70].

Measurements made on the observed surfaces were then used to determine the initiation of strain whitening. Changes in images, quantified with the aid of image-processing techniques was used to indirectly determine damage in the material. Additional observations at the surface of a polished sample under tension, and at the shear-banded

region of a fractured sample close to the fracture plane were made using the ODM. Lastly, a fracture surface was studied using scanning electron microscopy (SEM).

Strain point	Applied displacement [mm]	Applied strain
1	0.10	0.008
2	0.30	0.024
3	0.55	0.044
4	0.83	0.066

Table 2: Strain load points for observation with microscope

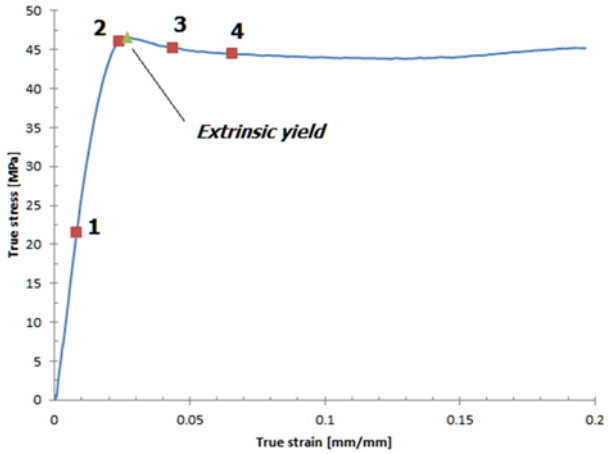

Figure 2: Quasi static tensile response in DP-460NS with observation points used for microscopy study

2.3 Image processing

Image segmentation was used to identify changes caused by strain whitening on the material surface while under tensile load. In the segmented images, white pixels can be considered as features of interest on the surface (defects, cracks, or changes from what is considered as the regular appearance), while the black pixels describe the background (non-strain whitened material in this case). For the image segmentation procedure, a fixed area of interest (AOI) was isolated on the observed surface at high magnification (500x). To assure that the same AOI was always studied regardless of strain; three features on the surface were used to define the corners of a rectangular area. The feature could be a crack, an inclusion or any other noticeable item on the surface image. The same features that defined the original AOI were selected in the captured images for a given sample once deformation was applied. For each AOI image, the file was first converted into an eight-

bit binary image, and then, segmented to separate features of interest (i.e. cracks, regions of stain whitening and shear bands) from the background. Segmentation requires the use of a threshold value, which can bias the results. For procedure consistency, segmentation was done using the IsoData algorithm included with Image J [71]. The IsoData algorithm was selected due to the automatic threshold implementation using histograms [72] and the good rankings (quality of results) that it achieves in different surveys [73–75].The implementation uses an optimal threshold to separate the image pixels into two different classes (object and background). The threshold initial guess is calculated by selecting a region of the image (its four corners) that is most likely to contain only points of the same class (background). The pixel values are averaged to obtain the initial threshold guess. A new threshold is calculated by averaging the integration of the values above and below the previous threshold. The process continues iteratively until the threshold value does not change any more. The image is then segmented into two separate classes using the optimized threshold value. Quantification of the number of black and white pixels after image segmentation determined the relative changes on the material surface. The ratio between the white pixels and the total amount of pixels was used to indirectly capture damage base on the surface changes from load point to load point

2.4. Traditional measures of damage

Damage was quantified using two traditional mechanical measures: changes in modulus of elasticity and effective stress during uniaxial tensile loading and subsequent unloading. The resultant stress-strain curves were used to calculate the material modulus of elasticity and to monitor the changes in effective stress. Load-unload measurements used the same test sample geometry as for the microscope observations. A universal hydraulic test machine with a calibrated load cell (Omegadyne model LC-412-500, Omega, Connecticut), a custom software control loop (LabVIEW, National Instruments, Texas) and an electronic controller (MTS FLEX, MTS, Minnesota) were used for the load-unload testing. The control loop made it possible to initiate the cycle at a fixed initial load point, strain the sample to the desired level and then unload the sample back to the initial load point, all under the same constant strain rate ($0.002s^{-1}$). Digital Image Correlation (DIC) [76] software (VIC-2D, Correlated Solutions [77]) was used to measure the test specimen strains using an optical extensometer. Images were captured using high-resolution DSLR cameras (NIKON D3200, 24.7 MP 23.2 x 15.4 mm CMOS sensor, Nikon Corporation, Japan), with a macro lens (SIGMA 105 mm 1:2.8 DG MACRO HSM, Sigma Corporation, Japan) and LED illumination (Lumahawk, AADYN technologies, North Carolina). Camera and illumination settings were fixed at the same value during the entire test (F8, 1/80 and ISO 1600 for the camera; 95% intensity with 25% temperature for the light source).

During load-unload testing, half of the gauge length of the test sample in the front view included a speckle pattern (Figure 1, bottom right hand) for monitoring strain on the surface of the material using the DIC. The uncoated half of the specimen permitted simultaneous macroscopic observations of the strain whitening changes. The load-unload procedure was conducted by loading the testing sample in tension up to a specified level of strain (displacement control) followed by an unloading cycle (displacement control with load monitoring). In between load cycles, the sample was taken out of the grips and the geometrical dimensions measured; this was done for two reasons. Firstly, this procedure ensured that the sample was unloaded entirely when reference measurements were made. Second, this allowed to account for permanent deformations, and adjust the applied strain for the next load cycle. In this manner, the total amount of applied strain at each cycle was consistent with the first loading. This ensured that no additional damage was introduced. The load-unload cycle was then repeated twice more for a total of three repeats for each test condition. At the beginning of each cycle, the sample was preloaded with a force of 10N to assure proper alignment and eliminate any slack in the grip. Due to equipment limitations in displacement control, caused by the control loop, the applied strain values for load-unload (Table 3) were slightly different from those used for microscopy (Table 2). Regardless of this limitation, the applied amount of strain for each load-unload condition correctly reflected three of the regions of interest used for the microscopic observations: linear-elastic, before yield, and just prior to the ultimate load.

Strain point	Target strain	Applied displacement [mm]	Actual strain
A	0.008	0.60	0.013
B	0.024	0.90	0.020
C	0.044	1.64	0.070
D	0.066	2.10	0.080

Table 3: Applied target strains for load-unload testing

When calculating damage using the stiffness of the material (Equation 4), the initial modulus of elasticity (E_o) was determined from the average of the first load cycle in the tested specimens at a particular deformation. The damaged modulus (E_u) corresponded to the average modulus measured during the first unload cycle for a given level of deformation. This follows the traditional convention for the measurements of damage in materials when using the modulus of elasticity [47]. The material modulus of elasticity was determined using the method described in ASTM E11-04 [78]. As previously mentioned load-unload has been investigated in the literature to quantify damage in polymers [17,49–51], but viscoelastic effects can present challenges when applying this methodology to polymers. Microhardness data [22] and a side study (Appendix Section A1), demonstrated that, for this particular material, long term visco-plastic effects were not significant. To minimize strain rate dependencies and viscoelastic effects, the load-

unload cycles were carried out under quasi-static conditions. Viscoelastic effects on the recovery portion of the unload cycle were initially considered as non-significant; however, the validity of this assumption was investigated by measuring the load response in subsequent load cycles.

When calculating damage from the strength data (Equation 5), the first measure of strength (first load cycle) and the last measure of strength (third load cycle) were used to define the strength of the material (σ) and the effective stress ($\bar{\sigma}$), respectively. For strain values above the extrinsic yield (e> 0.02), three load cycles were the maximum number of cycles that could consistently achieve the desired strain levels during testing. Therefore, this number of cycles was used to obtain data that could be subjected to statistical analysis. It was also assumed that after this small number of cycles, viscoelastic effects were eliminated and that the damage was stable.

3. RESULTS

3.1. Macroscopic strain whitening observations on the surface of a tensile specimen

During uniaxial load testing, DP-460NS showed strain whitening (Figure 3). A qualitative assessment of quasi static test images determined that as tensile load was applied , the material first developed small areas of a lighter color than the base material (e≤ 1.5%); the size of these areas also grew and coalesced with increasing strain evidencing further strain whitening (crazing) in the material (2% ≤e≤ 3%);. The development of white areas started well before the end of the elastic range (e~0.015) but the transition towards well-defined and oriented bands did not happen until reaching the maximum stress (45 MPa) and with strains well above 4%, although the strains were still below the average strain to failure (e~ 0.10) at this point. Localization of strain whitening was noted around the fracture zone of failed samples.

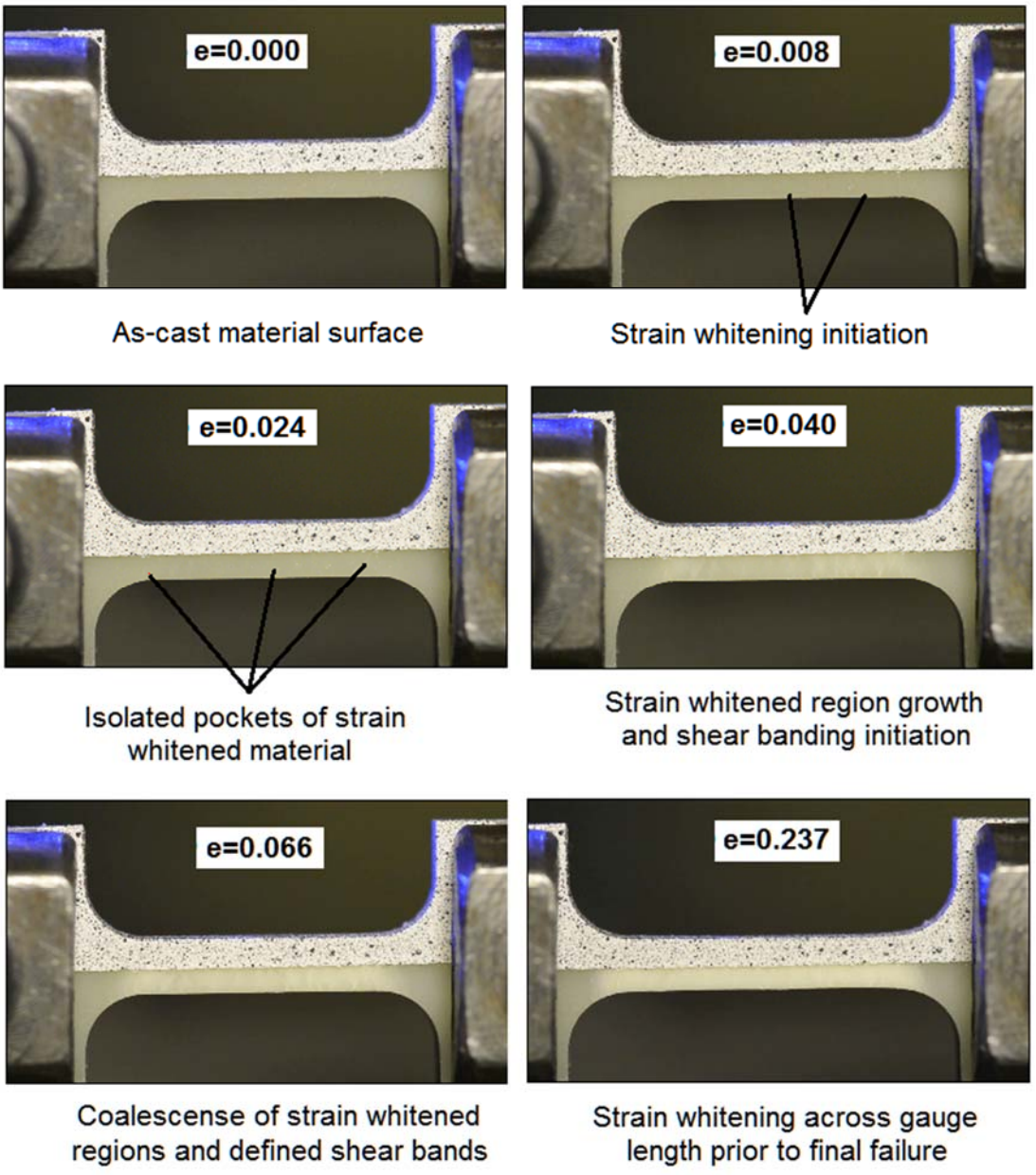

Figure 3: Macroscopic strain whitening in DP-460NS under tensile loading (0.002 s^{-1})

3.2. Microscope observations of test sample surfaces under tensile load

The material surface was observed under load using an opto-digital microscope. Initial observations at low level magnification (20 to 200x), identified that the observed strain whitening process along the gauge length of the specimen was similar to that observed macroscopically, although it was noted that initial surface changes at low levels of strain ($e<0.01$) were typically initiated at locations that included some sort of surface defect. The

source of these defects can be attributed to stresses caused by the curing and casting process. During curing the epoxy needs to go from a liquid to a solid state; this transition requires to physically accommodate the constituents in a given volume limited by the casting setup all of which introduces stresses in the material. For large magnification imaging (500x, Figure 4), the observations were concentrated in a small region of the test specimen gauge length. The typical crack evolution in the material (Figure 5, 1000x) can be described in the following manner: at low levels of strain ($e<0.008$, linear elastic region) the crack grew very slowly, from its original length of 8.4 μm to 11 μm. At higher strains ($e\sim0.024$, at or just before yield), the crack grew to approximately five times its length ($l\sim50$ μm) due to opening under load and coalescence with other cracks present in the vicinity. At this level of strain, the material whitening developed in small pockets around the boundary of the crack (Figure 5, image B). With increased levels of strain ($e\sim0.044$, above yield), the strain whitening grew and spread through the observed surface (Figures 4 and 5 image C). With further increases in strain ($e\geq0.066$, plastic region), the material transitioned to the formation of well-defined shear bands at a rough orientation of 30° relative to the vertical axis. Geometrical measurements, such as length and width, were made for a crack feature in two individual specimens (Table 4); the observations also included calculations for the resultant stress concentration factor k (Column 7, Table 4; Equation 1) and the stress at the tip (Column 8, Table 4).

Additional optical observations were made on the material using the ODM. On a polished sample (Appendix, Figure A-1), light scattering was detected at a particle (Diameter ~ 167 μm). The color change initiated within the particle and eventually extended beyond the particle boundary towards the epoxy matrix. The observed color change at the particle, which evolved with the strain load may be identified as cavitation.

ODM observations inside the shear band region after failure (Figure 6, top right hand) demonstrate the presence of a birefringent surface not observed in the unloaded and undamaged material (Figure 6, left hand). Micro-cracks (1 to 5 μm in length and less than1μm in width) and circular particles 3 μm to 20 μm in diameter) were observed in the shear-banded region (Figure 6, bottom right). Micro-voids on the surface (≤1 μm) were also present. The propagation of micro-voids and micro-cracks seem to be roughly oriented between 36 and 55°. Typical shear bands macroscopic orientation was measured between 26º and 30º. The observed shear band surface at high magnifications (Figure 6, bottom left) resembled porous material and was similar in appearance to cavitated material in other rubber toughened epoxies [34].

Although the fracture surface under SEM at various magnifications (Appendix, Figure A-2) resembles the typical appearance of a toughened epoxy with thermoplastic toughening [31], the morphology of the fracture resembles that of furrows and steps. According to Low and Mei [79], this type of morphology is evidence of crack growth and arrest, and it is similar to those observed in other toughened polymers [80]. No evidence of particle debonding, typically manifested by numerous black voids with a diameter roughly equal to the nominal size of the toughening particles, was evident in the SEM observations.

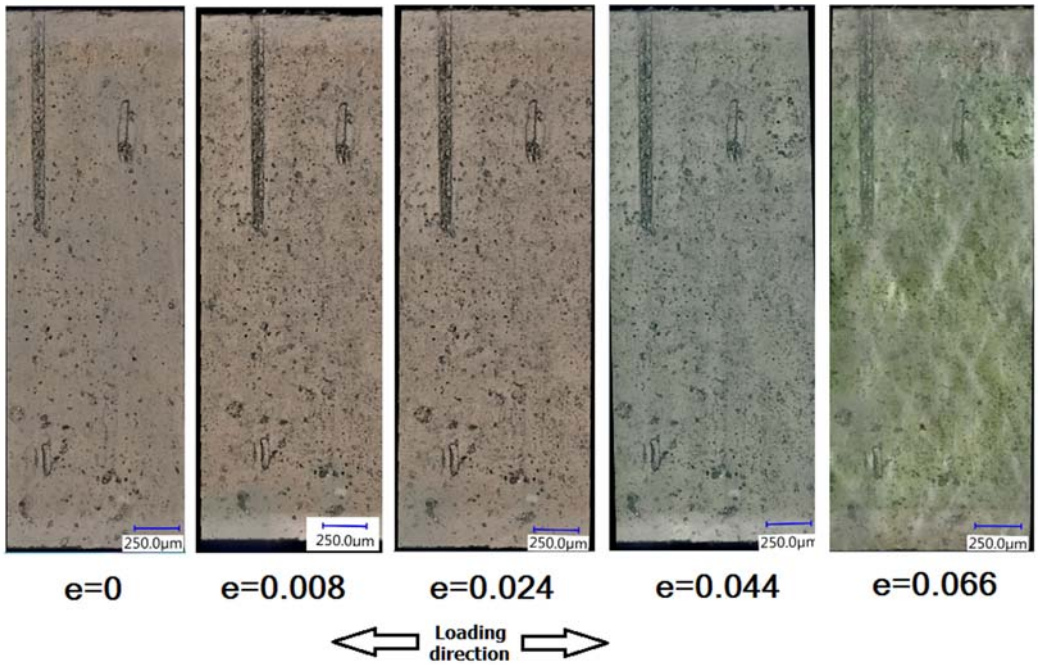

Figure 4: Strain whitening (crazing) in DP-460NS under tensile loading

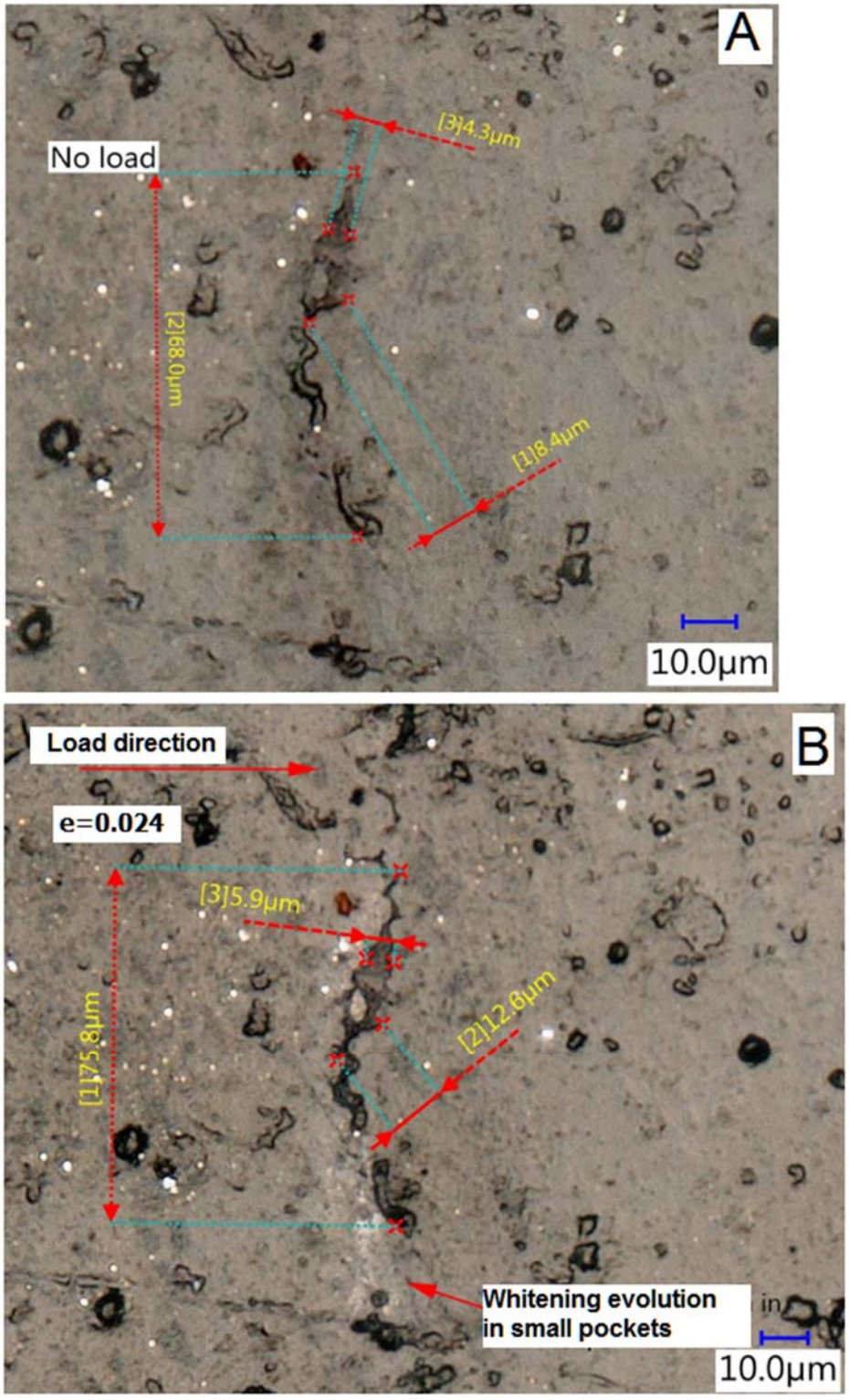

Figure 5: Evolution of a crack feature under tensile loading

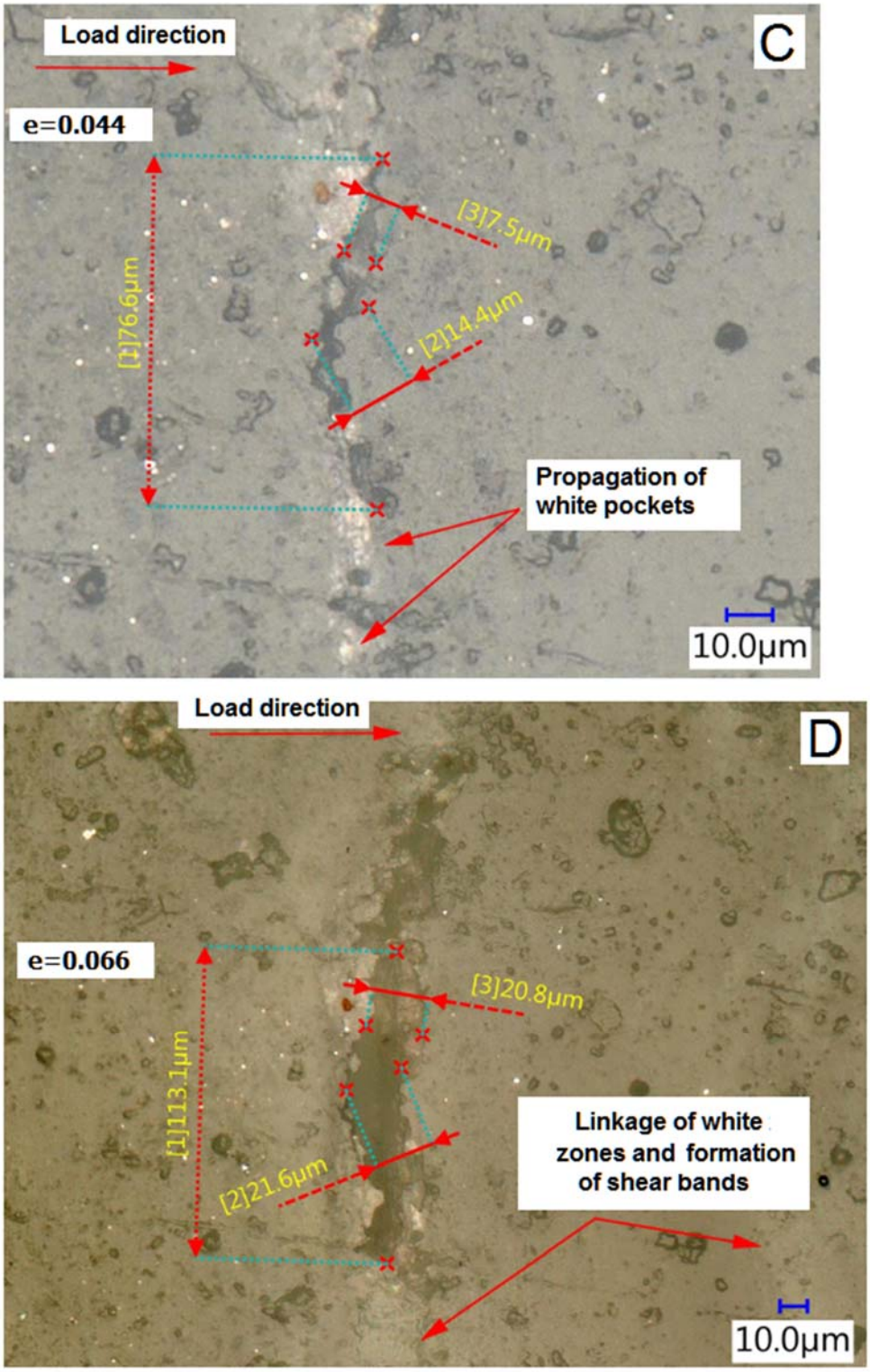

Figure 5: Evolution of a crack feature under tensile loading (continued)

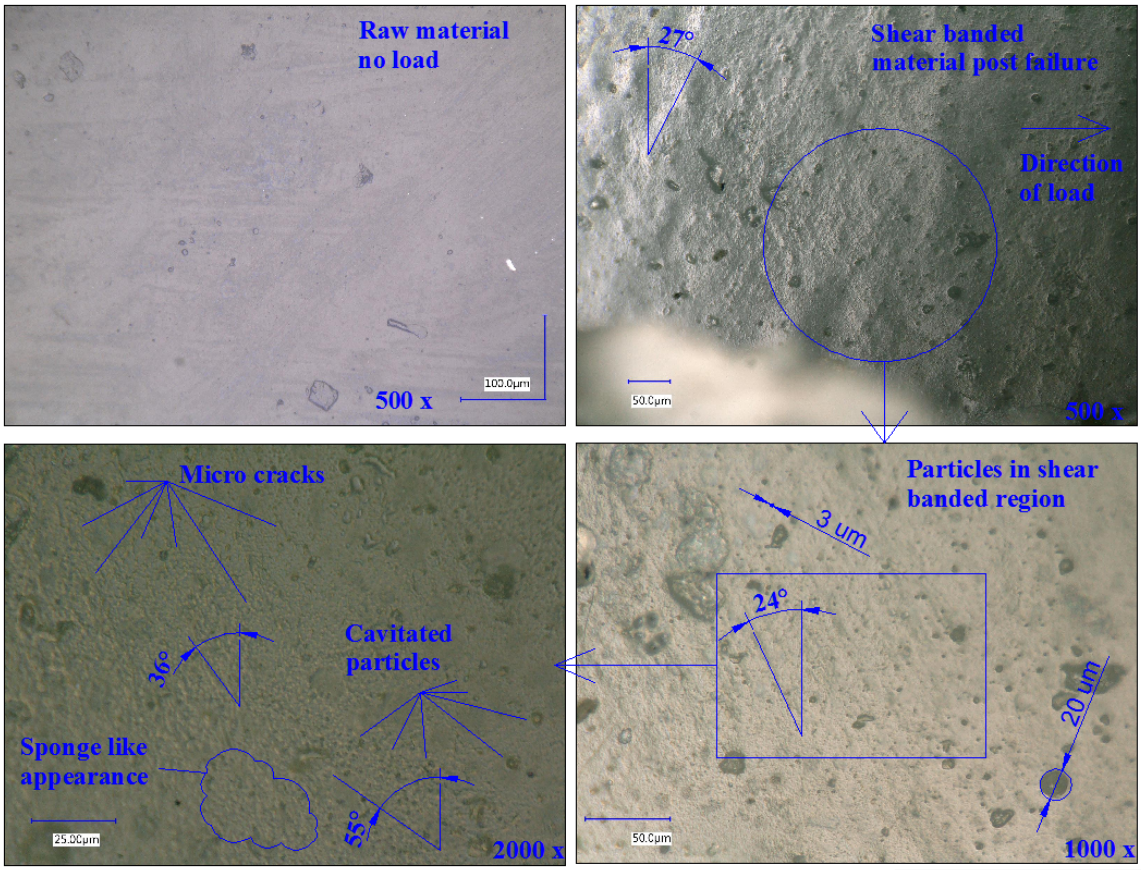

Figure 6: Observations of shear banded material. From top left in the clockwise direction: undamaged material. Shear bands after quasi-static tensile failure. Shear banded region at high magnification. Cavitated particles, micro-cracks and porous surface texture.

Sample	Strain	Av. stress σ [MPa]	Crack length (l) [µm]	Crack width [µm]	Tip radius (r) [µm]	*k* (Eq. 2)	Stress at tip (σ*k) [MPa]	Details
A-OM-2	0.000	0.0	8.4	~1.0	0.1	19	0.0	
	0.008	18.3	11.0	<2.0	0.1	22	402.0	
	0.024	38.6	50.0	< 6.0	1.0	15	584.0	Crack coalescence
	0.040	39.6	50.0	~7.5	2.0	11	436.0	
	0.066	39.4	130.0	~20.8	10.0	8	324.0	
A-OM-4	0.000	0.0	26.1	2.3	0.1	33	0.0	
	0.008	18.3	41.9	3.5	0.1	42	767.0	Crack coalescence
	0.024	38.6	100.0	3.8	1.0	21	811.0	
	0.040	39.6	100.0	2.3	1.0	21	832.0	
	0.066	39.4	100.0	2.9	2.0	15	597.0	

Table 4: Evolution of a crack feature in different samples under axial load

3.3 Tensile specimen surface, microscopic image analysis

Image segmentation was used to isolate the observed changes (i.e. crack openings and changes on the surface) caused by the applied strain on the material surfaces.. In the segmented images (Figure 6), the background (black pixels) can be considered as raw unchanged material, while the white pixels capture changes on the material surface. The number of black and white pixels in the images was monitored and provided a way to quantify the evolution of features on the material surface (Table 5). Additionally, the changes in overall AOI dimensions were used to provide a measurement of the local average engineering strain (Column 4, Table 5).

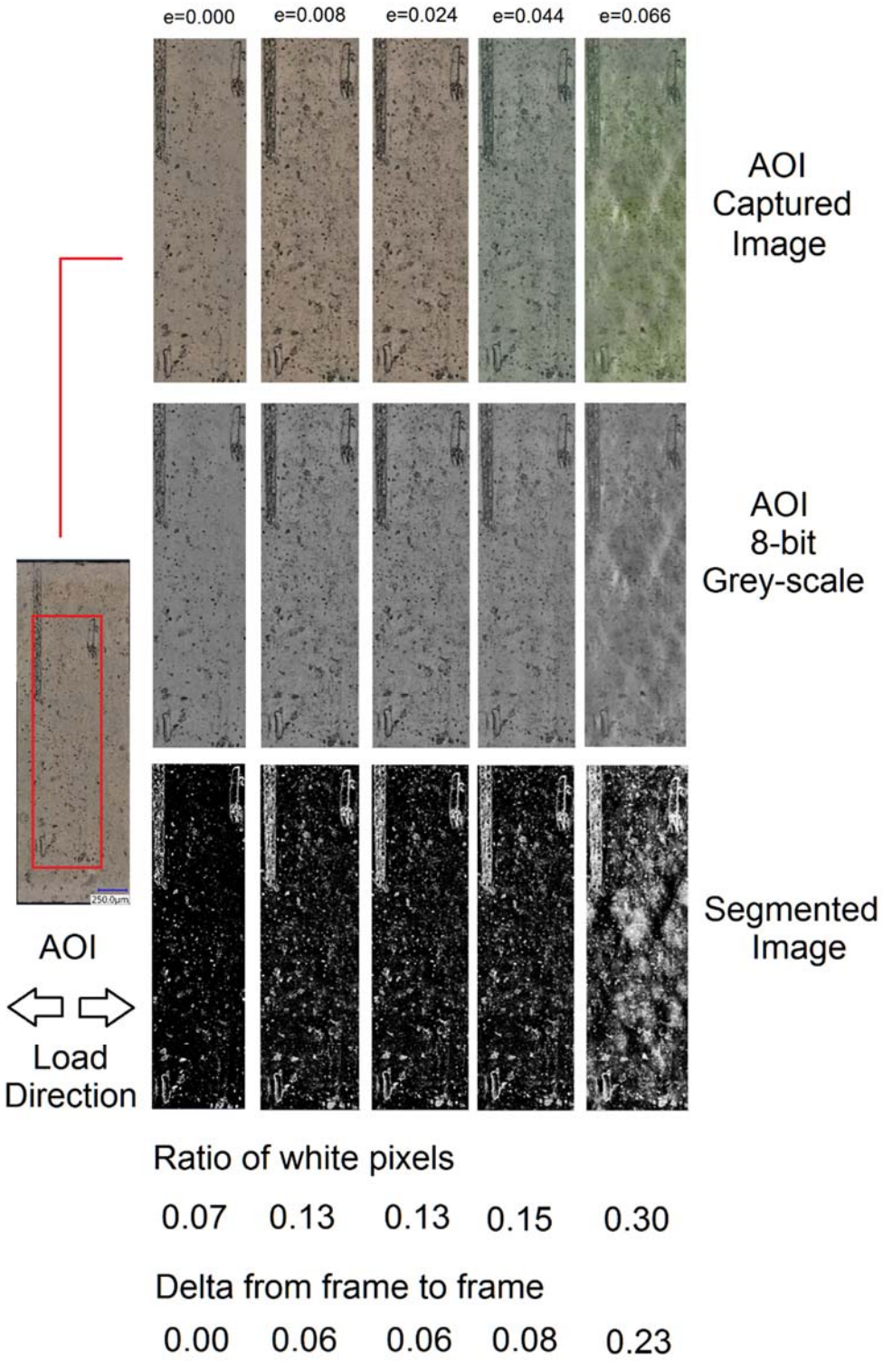

Figure 7: Segmented AOI regions in the material surface under ODM observation

Sample	δ [mm]	AOI Length x [µm]	AOI Width y [µm]	Local strain e_{xx}	Local strain e_{yy}	Binary Pixel count Black	Binary Pixel count White	Ratio White pixels to total pixels	D
A-OM-2	0.00	402.1	1,474.5	0.000	0.000	30,112,881	3,417,231	0.10	0.00
	0.10	438.2	1,555.1	0.090	0.055	30,468,682	4,075,958	0.12	0.02
	0.30	512.4	1,836.1	0.274	0.245	29,660,711	4,155,865	0.12	0.02
	0.55	440.0	1,595.3	0.094	0.082	26,053,675	7,632,821	0.23	0.12
	0.83	477.7	1,392.5	0.188	-0.056	21,926,007	8,902,953	0.29	0.19
A-OM-4	0.00	424.7	1,550.8	0.000	0.000	27,515,737	2,103,463	0.07	0.00
	0.10	591.4	2,112.1	0.393	0.362	26,452,977	3,831,823	0.13	0.06
	0.30	537.3	1,930.6	0.265	0.245	26,607,276	3,863,892	0.13	0.06
	0.55	449.8	1,537.5	0.059	-0.009	26,594,626	4,661,438	0.15	0.08
	0.83	464.4	1,536.8	0.093	-0.009	22,351,204	9,533,084	0.30	0.23

Table 5: Image binarization results at the AOI

Nucleation, opening, and coalescence of cracks caused surface changes, which manifested as whitening in the material. In addition, the presence of cavitation in large particles (diameter≥ 170 µm) was detected on a polished surface and inside particles within the shear-banded material (Appendix, Figure A-1). It could be possible, therefore, to obtain an empirical measure of damage. Changes between the segmented images could be construed as representative of the damage processes in the material, as observed on the free surface of the test specimen. The ratio between the white pixels and the total amount of pixels were used to represent the surface changes from load point to load point (Table 5, Column 9). Given that, the initial image contained features represented by white pixels; this initial value was subtracted from the calculated ratios to provide a measure of damage for each observed image (Table 5, Column 10). Using this empirical calculation, the predicted damage ranges from 0% up to 20% at the highest tested strain. Although there were changes in the AOI size from load point to load point, the total amount of pixels used for analysis was relatively unchanged (~ 3% in average), and it was considered that no significant error was introduced in the damage calculations.

3.4 Changes in modulus of elasticity and strength for load-unload and load-reload

3.3.

At low strains in the elastic region (e≤0.01, Figure 8, top), there was no strain whitening, and the material responded in a linear-elastic manner for all three load cycles. Prior to the extrinsic yield (e~0.02, Figure 8, second diagram from the top), incipient pockets of whitened material were observed, with a small change in the elastic response between cycles (6%), although the whitened material was more noticeable under magnification. At the next strain level (e~0.07, Figure 8, second diagram from the bottom), development of strain whitening was easily distinguished in the material. For this level of deformation, subsequent load events demonstrated a reduction of the linear-elastic region extent (from ~30 MPa at a strain of ~ 0.018 to ~12 MPa with a strain ≤0.01) followed by non-linear behavior. At strain levels closer to failure (e~0.11), the strain whitening propagated along the entire gauge length, and well-defined shear bands were recognizable at this stage (Figure 8, bottom diagram). The strain whitening process during load-unload was comparable to that described for a sample under tensile load until failure (Figure 3). Damage effects were also noted in the stress-strain response at high deformations: non-linear behavior in the unload portion of the load cycles; and changes in modulus of elasticity between the end of a cycle and the start of the next. Additionally, changes in the material strength between the first load cycle and the next were observed for strains beyond the extrinsic yield (e>0.07).Load-unload and load-reload measurements were made for the adhesive. The modulus of elasticity was calculated [78] from the experimental data for both the loading and unloading portions of the response. In general, the measured modulus of elasticity was well fitted to a linear response. The calculated coefficients of determination (r^2) were 0.99 on average (Appendix, Table A-3 to A-6). During unloading, the entirety of the measured response was considered. For the calculated modulus values in this region, the coefficient of determination fluctuated between 0.97 and 0.99. For all cases, the statistical coefficients comply reasonably well with the limits required by the standard: coefficient of determination (r^2=0.99) and coefficient of variation (V_1≤ 2%).
Changes in the modulus of elasticity values between load and unload cycles were detected with increases in strain (Figure 9). The modulus values are presented using box-whisker plots. Each box includes a horizontal white line to depict the mean value, black bars for the upper and lower fences, and 75% and 25% quartiles limit the box. The top row of graphs in the figure depicts the loading portion of the cycles, while the middle row summarizes the unload part of the experiments. At the two lowest strains tested (Columns A and B in the figure) there were no statistical differences in the data, but for strains greater than 0.069 (Columns C and D) there was a statistically significant change in stiffness (P-Value ≤$1.7x10^{-6}$, T-Test 95% confidence). The change can be described as a reduction in material stiffness between the first load and the first unload (~37.6% on average). After first unload, the subsequent unload cycles did not record further noticeable reductions in material stiffness and any differences in the recorded mean value of the unload slopes were not statistically significant (T-Test 95% confidence).Changes in stiffness between the successive loading portions of the cycles were also noted (Figure 9, first row, Columns C and D). On average, the typical decrease in stiffness between the first load and second load was 17%, while the stiffness decrease between the second and third load cycles was ~5.7%. Since there was a difference in the modulus of elasticity between first unloading (~1.17

GPa) and second load (~1.55GPa) in all cycles that include plastic deformations, the data suggest the presence of a short-term viscoelastic effect that induces recovery in the material. This viscoelastic recovery was no longer present after the second load cycle.

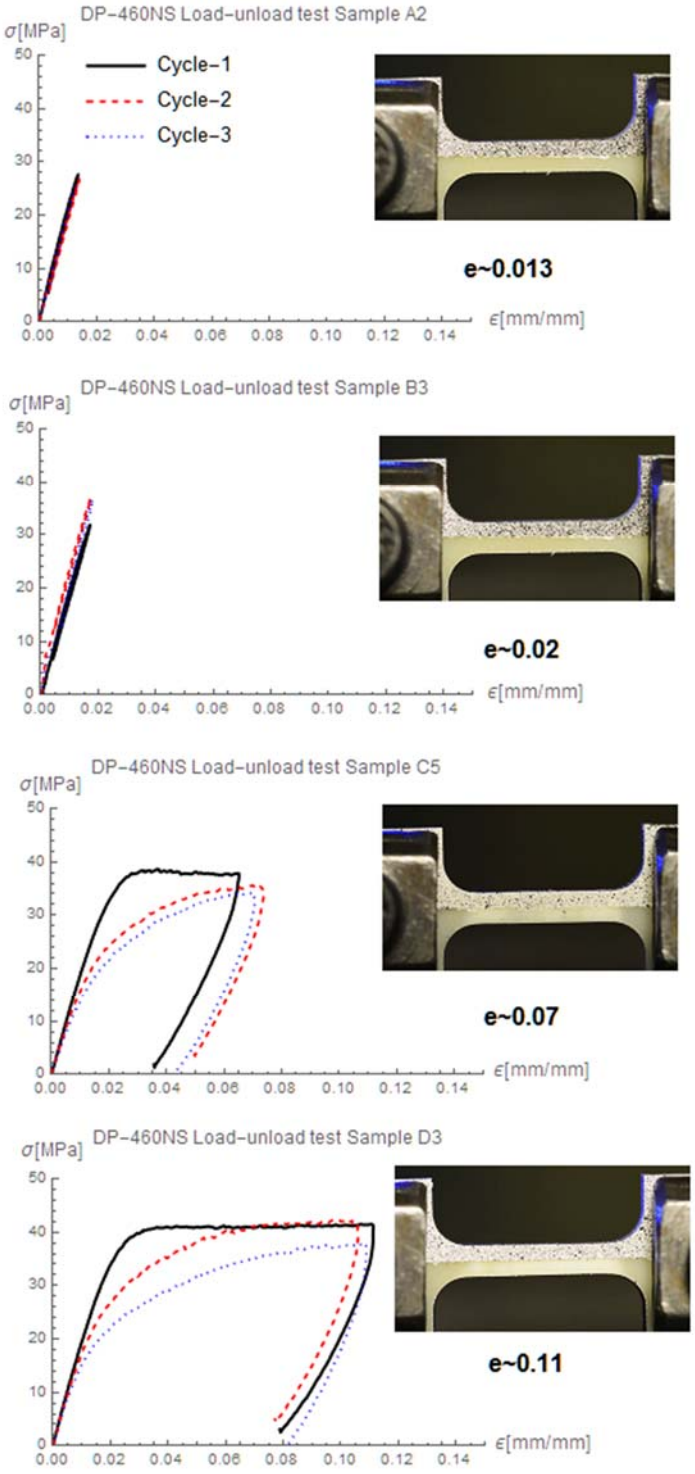

Figure 8: Typical load-unload curves and specimen images during load cycles

According to the stiffness data using first load (E_o) with first unloading (E_{u1}) in the traditional manner (Figure 10 left hand), no damage was present at the very low strains of the elastic region (e<0.013). At strains around the yield point (e~0.02), the damage was calculated as approximately 10%. For strains between the yield point and the first plastic deformation used ($0.02 \leq e \leq 0.07$), there was a sudden increase in damage, but the value stabilized at ~35%. Although the amount of average damage was unchanged at the next strain level (e~0.10, D~35%), there was a larger spread in the data; the upper fence value (D~47%) was higher than in the previous deformation point (e~0.07, D~40%). For strains above 0.069, it was considered that the material had damage saturation and no further increases in damage could occur. Although it can be said that saturation was caused by the applied number of cycles, the statistical analysis of the stiffness measurements does not support this, since:

1. The measured average stiffness between the second and third load cycle (Figure 8, top row), were statistically similar.
2. No statistical differences were detected in the unload stiffness between the first unload and subsequent unload cycles for the same amount of strain for any applied strain (Figure 8, middle row).

It can be concluded then, that the saturation was due to the applied strain level alone during the first load cycle.

Changes in measured strength were also quantified during load-unload cycles (Figure 9, bottom row of graphs). No changes in strength were detected in the elastic region (e~0.013). At strains near the extrinsic yield strength of the material ($e \leq 0.02$), there were no statistical differences (T-test, 95% confidence). At strains higher than the yield of the material and in the plastic deformation zone (Columns C and D), the detected changes in average strength were not statistically significant either. The lack of statistical significance was attributed to the large variability in the measured data (±6.3 MPa). However, the average strength decrease between cycles was calculated at approximately 5%.

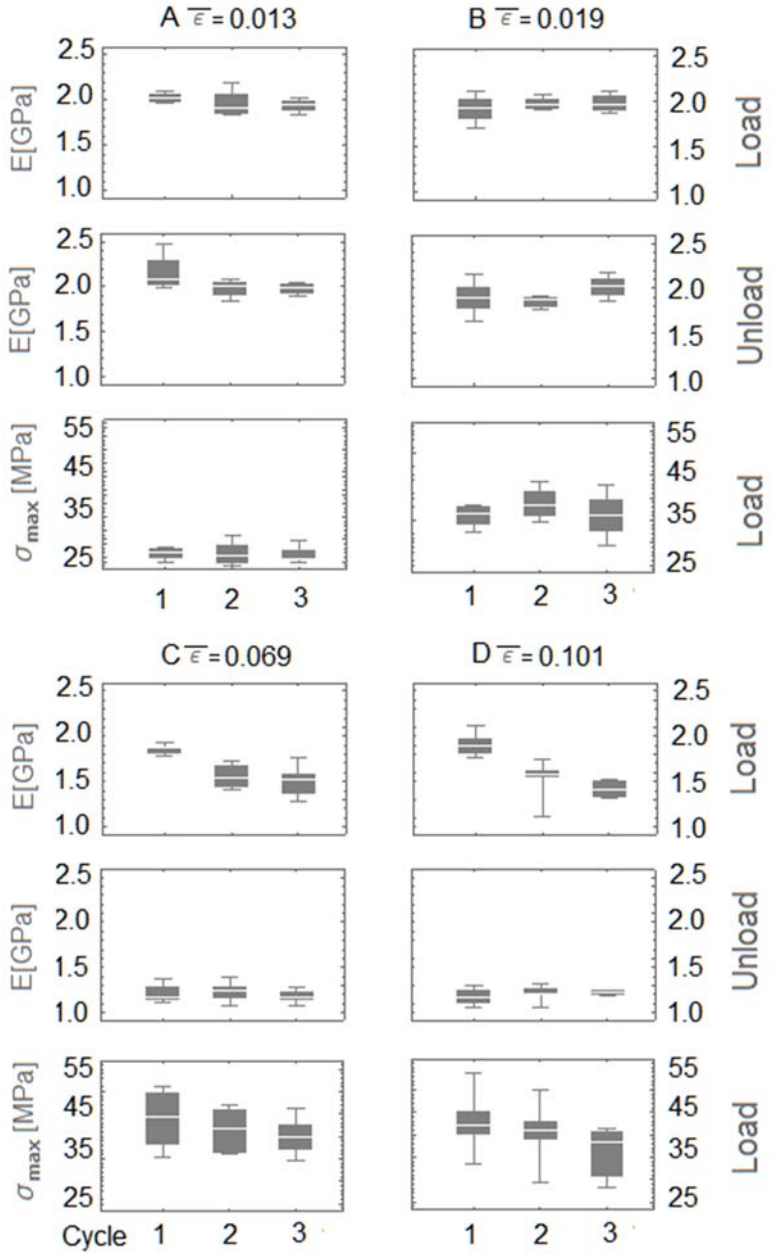

Figure 9: Measured changes in the material response for load, unload and reload cycles

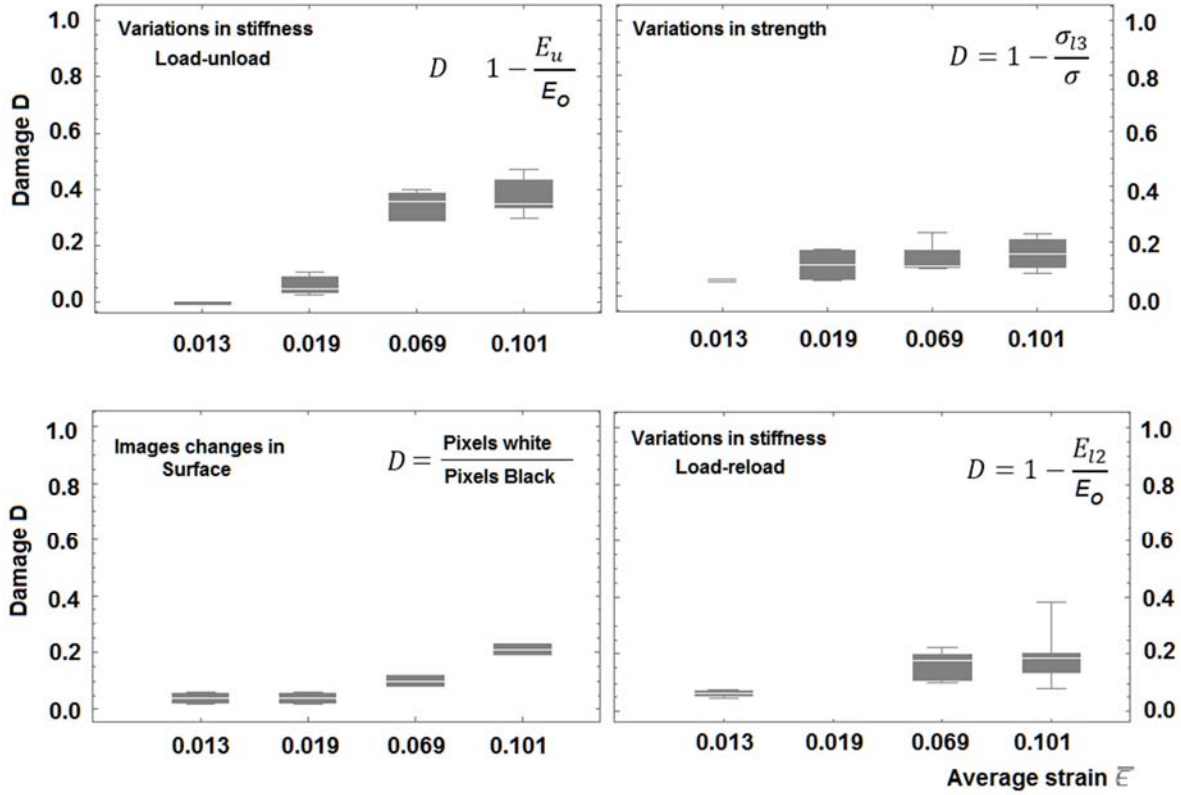

Figure 10: Calculated damage in the material

Since no fatigue effects were detected from the changes in modulus of elasticity, it was reasonable to assume that the changes in strength were caused by damage alone, and that the damage was induced in the material with the first deformation cycle. Variations between cycles can be explained by stabilization of damage. Damage was calculated using the difference between the measured strength in the first and third cycle. The damage evolution picture presented by the strength calculation (Figure 10, top right) was very different from that depicted by the changes in modulus of elasticity during load-unload. At low strains (<0.01) there was no damage, and the calculated value increased slowly with the increasingly applied strain. The damage value did not grow beyond 15–18% on average.

Damage values from the changes in microscopic surfaces were included for comparison (Figure 10, bottom left). Although it would be ideal to have a more significant sample size for statistical analysis (i.e. additional observations using more samples), the calculated values at the different strain levels were in agreement with the calculated damage from changes in strength. The damage values calculated from the changes in surface pixels were typically within one standard deviation of the average of the damage data from changes in strength.

The traditional damage calculation included viscoelastic effects in the unload portion of the cycle thus the calculated damage values overestimated the actual material damage. This viscoelastic effect was noticed as a recovery in the modulus of elasticity between first unload (1.17 GPa) and the second load (1.54 GPa). Damage calculations were repeated using the modulus of elasticity of the second load cycle (E_{l2}) to eliminate the viscoelastic effects (Figure 10, bottom right). In the linear-elastic portion of the material response (e=0.013) the recalculated damage value (~6%) was small and could be attributed to the statistical variations in the elastic modulus. At the next level of deformation (point B, e=0.019), meaningful damage data was not calculated (D<0) but for a single value of 10%. In the plastic deformation region (points C, e= 0.067 and D, e=0.101), the average damage was 16% and 19% respectively although there was much more variation at the largest strain tested (point D,± 9.1%) compared to the variation after the first onset of plastic deformation (point C, ±5.2%). The maximum damage value in the region of plastic deformations was 38.3% (upper fence, point D). The calculated damage figures using load-reload also describe damage saturation in the material during plastic deformation. The average damage values using load-reload, which minimize viscoelastic effects were in good agreement with the damage values calculated from strength variations and microscopic optical surface changes (Table 6).

Applied average strain	Damage ΔE (load-unload) ± one std. dev.	Damage Δσ ± one std. dev.	Damage Surface Changes (Average)	Damage ΔE (load-reload) ± one std. dev.
0.000	0.00	0.00	0.00	0.00
0.013	0.00	0.06±0.01	0.04	0.03±0.06
0.019	0.06±0.04	0.11±0.08	0.04	0.10
0.069	0.34±0.05	0.13±0.06	0.10	0.16±0.05
0.101	0.38±0.06	0.15±0.07	0.21	0.17±0.08

Table 6: Average damage values calculated by all methods

4. DISCUSSION

4.1. Microscope observations and optical measurements on the specimen surface

The microscope imaging demonstrated that the material developed strain whitening under load, followed by the development of shear bands. Of importance is the fact that the polished surface observation demonstrated micro-cracking and whitening inside and around an embedded particle (~165 μm in diameter), confirming the presence of cavitation like behavior with increases in strain. SEM analysis revealed the existence of a mechanism for crack arrest, as evidenced by the presence of furrows and steps. The images also

discarded the possibility of particle debonding since there was no significant evidence of concave regions with circular or ellipsoidal perimeters with a diameter roughly equal to that of the embedded particle used for toughening. Observations inside a shear-banded region at high magnification demonstrated a porous like surface appearance and the presence of micro voids. Such descriptions are similar to those of cavitated particles in rubber modified epoxy resins as presented by Yee and Pearson [34]. Therefore, it can be assumed that cavitation was the primary damage mechanism in the material. It was possible to calculate the theoretical stresses required to initiate strain whitening by cavitation (Equations 1) and to compare those values against the stress concentrations calculated from the measured crack feature in the microscope images (Table 4). One limitation of this approach is the fact that the calculations (Equation 1) describe a volumetric process while the approximated stress values used a free surface. We considered that the stress field on the free surface was representative of the stress field in the surrounding material.

Equation 1 predicted a stress value to initiate a cavitation process in the order of 120 to 360 MPa (for particles between 1mm and 0.5μm in diameter and assuming E~120 MPa). However, the stress range for cavitation can be affected by the chemical composition of the toughening phase. For example, the required cavitation stresses for butadiene particles (E~1-2 GPa) predicted by Equation 1, could be in the range of 1000 to 6000 MPa while cavitation for silicon rubber (E~1 MPa) [81], can occur at stresses as low as 1 to 3 MPa.

An average of the crack tip stresses (Table 4, Column 8) was used to approximate the stress field around areas of stress concentration. The calculated average (402 MPa) is certainly high enough to satisfy the stress state that can promote internal cavitation (Equation 1, 120-360 MPa). As further verification, a balance calculation (Appendix, Section A4) between the strain energy and the energy required for a phase transition (from solid to viscous), also predicted that material cavitation was possible. Although Equation 1 and the balance calculation are in agreement, this only serve as a first approximation. It has to be acknowledged that the calculated stress values are high for polymers, in the order of 400 MPa, and comparable in magnitude to that of the yield in metals. A fracture mechanics analysis using the stress intensity factor and the derived stress field around a crack tip, may provide a better insight into this problem. This will be consider for future analysis. Even though the proposed analysis is limited, of importance is the fact that even at low strains (e~0.008, well within elastic deformation), the stress concentrations in the material adjacent to a crack as a small as 11 μm in length and with a tip radius less than 2 μm, can be high enough to start the cavitation process in particles with diameters larger than 0.5 μm. The small amount of detectable whitening (surface change ≤ 13%, Table 5) observed in the material under high magnification, provides supporting evidence for strain whitening initiation at low levels of load. As a contrast, the variations in stiffness from load-unload did not detect any damage at low strains, but this can be explained by lack of sensitivity and differences in scale between the two methods.

By using image processing during the formation of shear bands, it was possible to determine that the initiation of the shear bands corresponded to areas where strain

whitening and crack growth was present (Figure 11). From the analysis in the measured data, the stress at the crack tips was high enough, compared to that of the surrounding material, to cause cavitation, develop plastic zones and induce differences in gradients that later on, could favor the formation of shear bands. The local average strain measurement in the AOIs (Table 5, Columns 4 and 5), when compared against the applied average strain, also provide evidence of non-uniform strain distributions in the material.

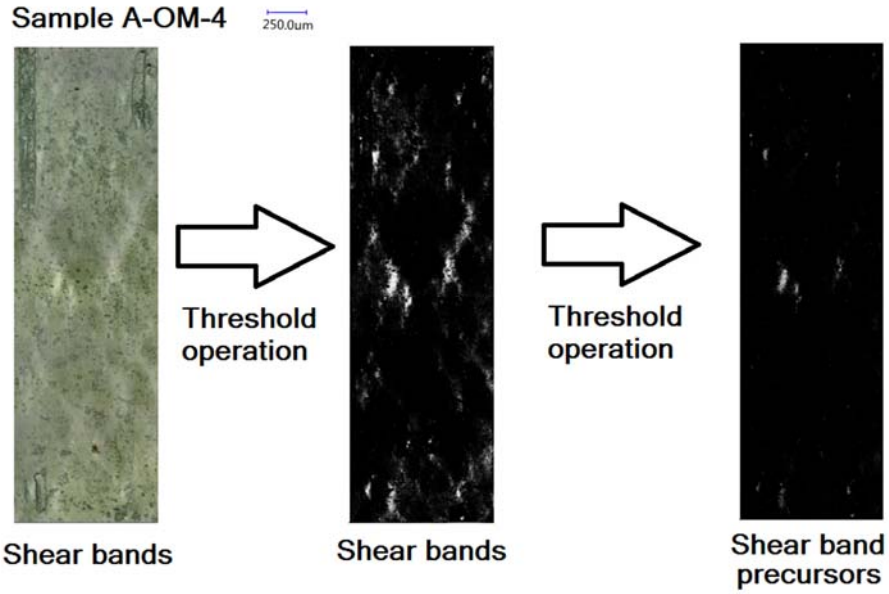

Figure 11: Pockets as precursors for shear bands

4.2. Changes in modulus of elasticity in the material

At strains well below the yield point and in the linear-elastic region, no statistically significant (T-test 95% confidence) changes in stiffness between load cycles or between consecutive load and unload could be detected, demonstrating that no damage was induced in the material. With increases in strains up to around the yield point ($e \leq 2\%$), no statistically significant changes in stiffness could be detected either. In this strain region, insipient strain whitening was the only phenomenon detected in the material although not enough damage was induced to cause noticeable changes in stiffness. With further increase in strain and within the initiation of plastic deformations ($0.02 < e \leq 0.07$), a significant drop in stiffness (Figure 9, Column C) between the first load cycle and the subsequent second load cycle was measured (18% drop) but no changes in stiffness between the second and third load cycles. P-values much smaller than 0.05 (0.0054 and 0.0028, T-Test 95% confidence) pointed to the statistical significance of the initial change. Strain whitening was the dominant phenomenon detected in this region, and the opening and propagation of cracks besides particle cavitation could account for the softening of the material

response and the calculated damage. For strains well beyond yield of the material and with significant plastic deformation ($e \geq 0.07$), no additional drop in the stiffness was detected, but the material showed a significant transition towards shear banding. At these levels of strain, there were two distinct responses in the unloading curve (Figure 12). The first portion of the unloading was stiffer (dashed red portion), followed by a transition to a lower stiffness (dotted blue portion). It can be noticed that the respective values for modulus of elasticity (red whisker box and blue whisker box, Figure 12 bottom part) were quite distinct among each other and significantly different from the modulus of elasticity measured in the undamaged material (light gray, Figure 12 bottom part).

One possible explanation is that the observed behavior can be explained in terms of chains and molecular structure in polymers. At low strains, the material first exhausts easily breakable Van der Waals bonds; this allows the polymeric chains to slip and rotate among each other, and then micro-cracks open to accommodate the deformations. This initial description of the deformation process was derived from basic principles in regards to atomic bonds [82], the basic molecular structure that can be used to describe polymeric materials [83] and descriptions by authors like Bowden [70], Argon [84] and Boyce [85,86]. With further straining, the material develops more openings, although they are governed by particle cavitation and/or development of localized plastic zones; eventually, the material transitions towards shear banding due to the high stress gradients that develop between cracks.

The development of high stress gradients between cracks has been previously reported in the literature [87,88], as well as the transition between cavitation and shear banding in reinforced polymers with elastomeric materials [35,36]. While this is happening, further chain slipping occurs and eventually the covalent bonds that interlink chains need to be broken to allow further deformation. In the end, the chains are uncoiled and aligned, and only strong crosslinks that interconnect the main chemical compounds inside the chains are available to support the loading prior to final fracture. When the load direction is reverse just before fracture, the material needs to re-accommodate all the strong bonds first. Hence the brief stiff response detected. Once the principal bonds are repositioned, the unloading process needs to close openings and slide chains relative to one another, which is a process that requires much less force. This process matched the observed behavior described in Figure 12. In this figure, with the increase in strain and load cycles, the stiffness to return the material back to the unload condition increased, but this was followed by a constant softer portion in the unloading process. For both portions of the unloading curve the coefficient of correlation was very high (0.97 to 0.98), therefore they can be independently described by linear regression, although the calculated coefficients of variation increased up to 6% in the stiff section of the curve.

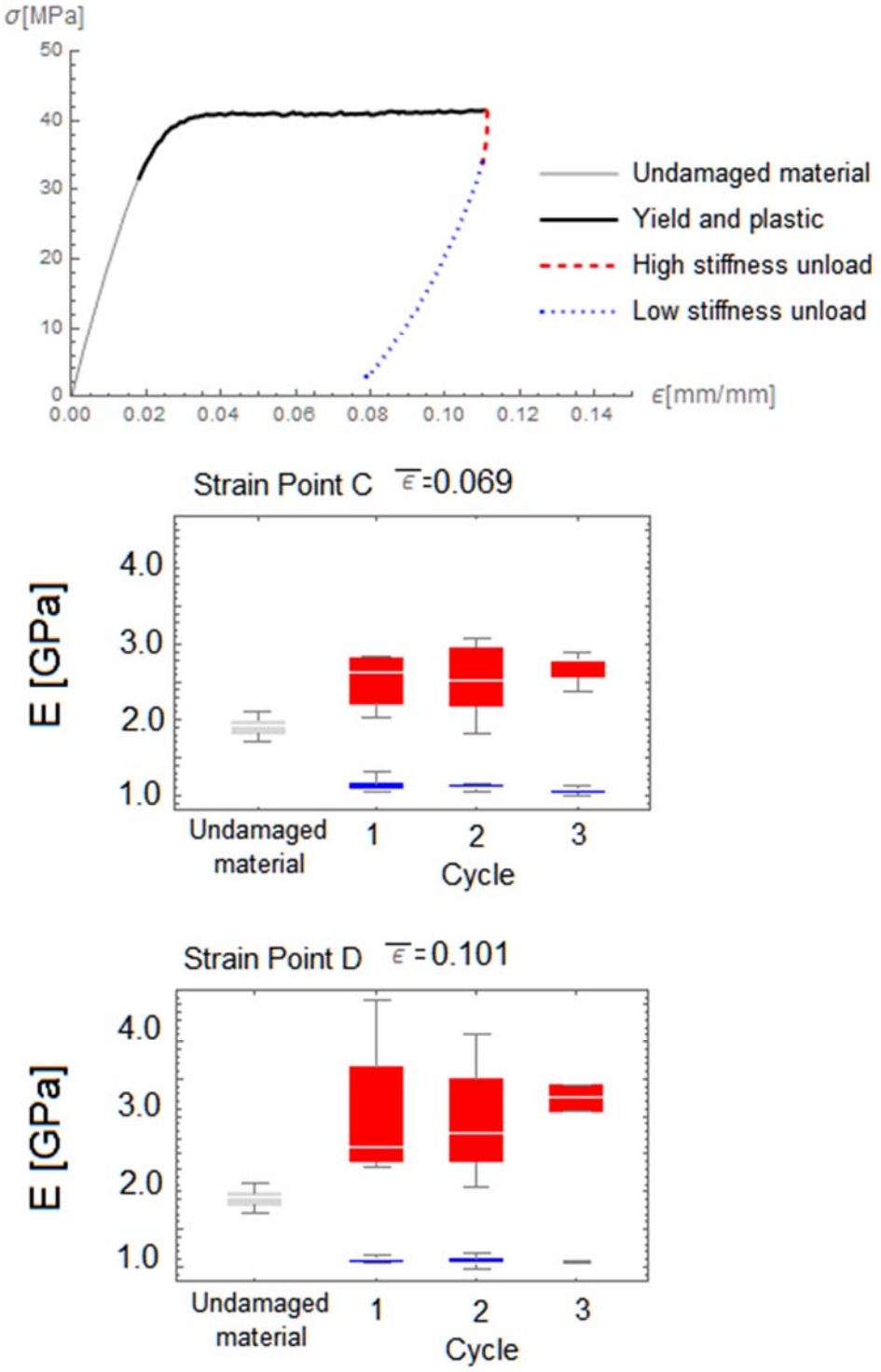

Figure 12: Unload response differences in modulus of elasticity

4.3. Calculated material damage

A series of load-unload cycles to determine changes in modulus of elasticity were conducted. The data provided a baseline measure to qualify the observed changes in the material surface during uniaxial tension. Damage was calculated for all experimental methods (Figure 10 and Table 6). The damage process can be accurately described with the use of sigmoidal functions.

For the changes in stiffness with load-unload (Table 7, first row; Figure 13 blue solid and dot markers) the sigmoidal curve predicts a damage value around 40% for saturation. The damage starts developing when the strain reaches a value in the plastic regime of deformation (e=0.04) and grows very quickly.

Damage calculated from the strength increased up to a value of 15 to 18% on average and a calculated maximum of 22%. The calculated damage can also be represented by a sigmoidal function (Table 7, middle row; Figure 13 red dashed with square markers). In principle, both methods (stiffness and strength) should predict similar results. In this situation, the discrepancy can be explained by the presence of a short-term viscoelastic effect. Once the viscoelastic effect was considered, by modifying the damage calculation with the use of the stiffness value of the second load rather than the first unload, the calculated average damage was 16 to 19%, with a calculated maximum of 38%. The calculated damage excluding viscoelastic effects was also well described in terms of a sigmoidal function (Table 7, bottom row; Figure 13 purple dotted and diamond markers).

Method	**Sigmoidal model**	**r^2**
DΔE load-unload	$\frac{0.38}{1 + exp^{16.34-271\varepsilon}}$	0.98
DΔσ	$\frac{0.15}{1 + exp^{4.32-296\varepsilon}}$	0.99
DΔE load-reload	$\frac{0.18}{1 + exp^{3.04-175\varepsilon}}$	0.99

Table 7: Damage data (Figure 10), sigmoidal function curve fit

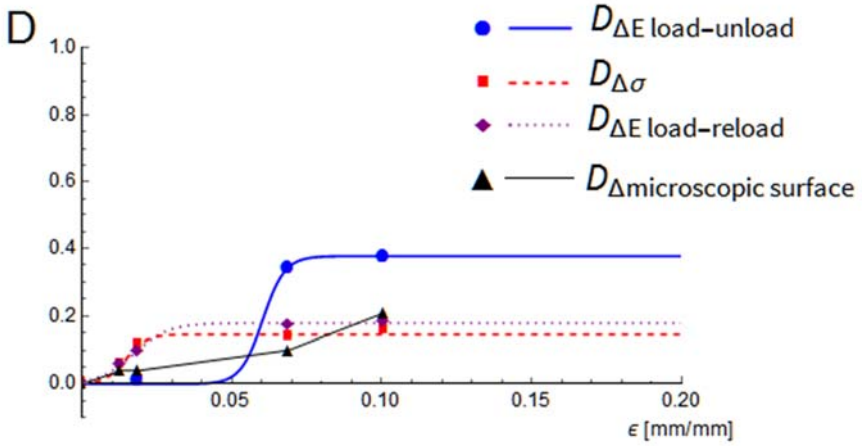

Figure 13: Damage data average values vs. sigmoidal functions (Table 7)

The damage predicted by changes in microscopic surface could not be fitted to a sigmoidal response (Figure 13 black solid line and triangle markers). More sample points that can better describe the spread at each strain point may be required to fit a proper curve to this data. With the current information the behavior is well described by three different linear regions. Nevertheless, the values align well with the measurements from changes in strength and the corrected calculation for stiffness at low strains (e=0.01) and high strains in the plastic region (e>0.07) although is not possible to infer, from the data, the actual saturation detected by the other methods.

From the microscope observations and the measurements of stiffness and strength, crack opening, small plastic zones and cavitation emerged as the most likely and significant damage mechanisms in the material up to well with-in plastic deformation (e≤0.07). At higher strain, the formation of shear bands was more significant. Shear bands cannot be classified under the traditional definition of damage (opening and coalescence of voids); however, there was optical evidence of the presence of micro-cracks, micro-voids and cavitated particles inside the shear-banded regions. In addition, it is necessary to consider that the shear-banding process influenced the material stiffness during the unloading response. The impact was more significant at the last stages of deformation, prior to failure in the material. Traditionally, shear bands are oriented at 45°; in the observed surfaces, the shear bands were oriented between 30° and 40°. It is possible that the presence of micro-cracks and particle cavitation in the disperse phase and/or the chemical composition and chain structure of the material influenced the shear band orientation, but determining this with certainty would require further investigation. However, Yee and Pearson [34], reported that variations in shear band orientation from 45º could be expected due to the presence of plastic zones and dilatation.

5. CONCLUSIONS

A toughened structural epoxy adhesive (DP-460NS 3M, Minnesota) was used to measure damage developed during uniaxial tensile loading at different strain levels. Microscope observations confirmed that the material developed strain whitening due to crack opening and particle cavitation and these mechanisms were followed by shear banding in the later stages of deformation (e> 0.04). The shear banding developed from areas that were initially strain whitened. Crack features were monitored and measured during the deformation using microscopy. Typical crack lengths grew approximately 10 times in size (from ~10 up to ~100 μm) while the crack width was relatively constant and rarely grew larger than 10 μm. The crack length and tip radius were used to calculate stress concentration factors. The average stress concentration factor (~20) was in good agreement with those proposed by Patterson (~25) and comparable to those (10 to 50) that can be expected by a polymer that crazes as described by Gent. Patterson's theoretical stress concentration value is a good rule of thumb still applicable today for modern epoxy adhesives. However, the calculated levels of stress using stress concentration are high for polymeric materials, the analysis needs further review using fracture mechanics principles. Nevertheless, the low range of concentrated stresses in the test samples (300 to 400 MPa) were in relative agreement with Gent's theoretical stresses to initiate cavitation in this material (120 to 360 MPa), although the range values from Gent's approximation are highly dependent on the exact value of the modulus of elasticity used for the calculation.
Importantly, it was possible to cause cavitation at relatively low levels of stress (~10 MPa), which is well within the elastic response of this adhesive material. Although the initiation of strain whitening can be influenced by many factors (e.g., chemical composition, associated state of stress) and may not be extrapolated as a general behavior of all toughened epoxies, potential damage in the adhesive at low levels of stress can change the assumed integrity, performance and life expectancy of bonded components. This is yet another complexity that needs to be evaluated when using structural adhesives.

Traditionally, damage measurements are conducted with load-unload testing. This method proved to be effective if the viscoelastic effects are considered. This type of test required the use of multiple samples and was time-consuming for both physical testing and data processing. Further, the measurement of the modulus was made along the gauge length of the tested samples with a virtual extensometer. Although large gradients were not detected in the DIC results, this approach can only give an average representation of the damage in the material because it does not consider localization phenomena or the changes that occur around the final fracture zone. For materials with large localizations, the damage distribution along the gauge length will be required to characterize the damage process adequately. Microhardness has been explored for this task [22], but it has limitations as the micro-indentations will introduce deformations and additional stress concentrators in the material surface that could skew damage measurements between load cycles. In this work, the changes in material surface (strain whitening and shear banding) were directly linked to damage using an empirical method. The damage was approximated by measuring the changes in image pixel ratios after image segmentation. The calculated damage values were within one standard deviation of the average damage calculated from changes in effective stress. Although the empirical optical method can be used to characterize damage

evolution at different locations along the gauge length, implementing this is not practical. The measurements must be conducted in a small area of the material (field view limitation of the microscope) at a specific time in the load history and could require extensive periods of time to complete any image capturing required, which in turn introduces the potential for creep. A natural progression of this work will be the development of an optical method using macroscopic images to continuously measure damage along the specimen gauge length.

Changes in modulus of elasticity and the effective stress in the material were monitored between loading cycles. Changes in stiffness were linked to the presence of strain whitening as well as shear banding. Although the damage calculated using the changes in effective stress was substantially lower (D~18%) than predicted by traditional changes in stiffness (D~35%), the differences were reconciled by accounting for short term viscoelastic effects. The damage figure was recalculated using the load and reload slope (D~19%). This last value was in agreement with the changes in effective stress (D~15 to 18%) as well as the microscopic changes in the material surface (D~21%). The differences in the stiffness of the material caused by viscoelastic effects could be of vital importance for constitutive models that incorporate damage in their formulation. The results indicate that, to predict the behavior of the studied adhesive (DP-460NS), the implementation of a constitutive model with damage needs to be capable of differentiating between load and unload scenarios. The observed types of behavior influencing the effective damage, which are the role of micro-cracks, plastic zones, and cavitated material, cannot be overlooked in the characterization of structural epoxy adhesives.
A natural progression of the microscopic observations is to quantify macroscopic measurements and potentially relate them to damage. Chapter 6 describes the development of a measuring technique that can quantify strain whitening at the macroscopic level, and correlate the measurements with material damage.

Acknowledgements: The authors would like to thank 3M Company, Initiative for Advanced Manufacturing Innovation and Automotive Partnerships Canada for financially supporting this research. The authors gratefully acknowledge Jeff Wemp, Jason Benninger, Chris Tom and Neil Griffett for their assistance in sample manufacturing and adhesive material testing.

REFERENCES:

[1]
VW, FIAT, RENAULT, OPEL, DAIMLER, VOLVO. SuperLight Car program n.d.;2013. http://www.superlightcar.com/public/index.php.

[2] Multi Material Light-weight Vehicle 2013.

[3] Lightweight Vehicle Structure Conference. Innov. Dev. Light Weight Veh. Struct., Wolfsburg, Germany: VolksWagen Group; 2009.

[4] Cui X, Zhang H, Wang S, Zhang L, Ko J. Design of lightweight multi-material automotive bodies using new material performance indices of thin-walled beams for the material selection with crashworthiness consideration. Mater Des 2011;32:815–21. doi:10.1016/j.matdes.2010.07.018.

[5] Symietz D. Structural Adhesive Bonding: The Most Innovative Joining Technique for Modern Lightweight Design, Safety and Modular Concepts -Progress Report-. - 2005. doi:- 10.4271/2005-01-1747.

[6] Fay PA, Suthurst GD. Redesign of adhesively bonded box beam sections for improved impact performance. Int J Adhes Adhes 1990;10:128–38. doi:DOI: 10.1016/0143-7496(90)90095-F.

[7] Kinloch AJ. Fracture behaviour of polymers. London: Applied Science Publishers; 1983.

[8] Adams RD, Harris JA. The influence of local geometry on the strength of adhesive joints. Int J Adhes Adhes 1987;7:69–80. doi:10.1016/0143-7496(87)90092-3.

[9] Belingardi G, Goglio L, Tarditi A. Investigating the effect of spew and chamfer size on the stresses in metal/plastics adhesive joints. Int J Adhes Adhes 2002;22:273–82. doi:DOI: 10.1016/S0143-7496(02)00004-0.

[10] Wang CN. On the fracture of constrained layers. Int J Fract 1998;93:227–46.

[11] Meng Q. Nanosilica-toughened polymer adhesives. Mater Des 2014;61:75–86.

[12] Khalil AA, Bayoumi MR. Effect of loading rate on fracture toughness of bonded joints. Eng Fract Mech 1991;39:1037–43.

[13] Raghavan D, He J, Hunston D, Hoffman D. Strain rate dependence of fracture in a rubber-toughened epoxy system. J Adhes 2002;78:723–39.

[14] Georgiou I, Ivankovic A, Kinloch AJ, Tropsa V. Rate Dependent Fracture Behaviour of Adhesively Bonded Joints. Eur Struct Integr Soc 2003;32:317–28. doi:http://dx.doi.org/10.1016/S1566-1369(03)80105-X.

[15] Akhavan-Safar A, Barbosa AQ, da Silva LF, Ayatollahi MR. Micro failure

analysis of adhesively bonded joints enhanced with natural cork particles: Impact of overlap length and particles volume fraction. Frat ED INTEGRITA Strutt 2018:266–74. doi:10.3221/IGF-ESIS.46.24.

[16] Gilat A, Goldberg RK, Roberts GD. Strain rate sensitivity of epoxy resin in tensile and shear loading. J Aerosp Eng 2007;20:75–89. doi:10.1061/(ASCE)0893-1321(2007)20:2(75).

[17] Balieu R, Lauro F, Bennani B, Haugou G, Chaari F, Matsumoto T, et al. Damage at high strain rates in semi-crystalline polymers. Int J Impact Eng 2015;76:1–8. doi:10.1016/j.ijimpeng.2014.08.013.

[18] G'Sell C, Hiver JM, Dahoun A. Experimental characterization of deformation damage in solid polymers under tension, and its interrelation with necking. Int J Solids Struct 2002;39:3857–72. doi:10.1016/S0020-7683(02)00184-1.

[19] Lauro F, Bennani B, Morin D, Epee AF. The SEE method for determination of behaviour laws for strain rate dependent material: Application to polymer material. Int J Impact Eng 2010;37:715–22. doi:10.1016/j.ijimpeng.2009.11.007.

[20] Park C, Huh H, Kim J, Ahn C. Determination of true stress-true strain curves of polymers at various strain rates using force equilibrium grid method. J Compos Mater 2012;46:2065–77. doi:10.1177/0021998311429882.

[21] Lopez J. Microhardness Testing of Plastics : Literature Review 1993;12:437–58.

[22] Trimiño LF, Cronin DS. Damage measurements in epoxy structural adhesives using microhardness. Int J Adhes Adhes 2018;82:211–20. doi:10.1016/j.ijadhadh.2018.01.014.

[23] Dufour L, Bourel B, Lauro F, Haugou G, Leconte N. International Journal of Adhesion & Adhesives A viscoelastic - viscoplastic model with non associative plasticity for the modelling of bonded joints at high strain rates 2016;70:304–14. doi:10.1016/j.ijadhadh.2016.07.015.

[24] Bernal CR, Frontini PM. Determination of fracture toughness in rubber modified glassy polymers under impact conditions. Polym Eng Sci 1995;35:1705–12.

[25] Kinloch, A J; Shawn, S.J.; Hunston, D.L.; Tod DA. Deformation and fracture behaviour of a rubber-toughned epoxy: 1. Microstructure and fracture studies. Polymer (Guildf) 1983;24:1341–54.

[26] Schirrer R, Fond C, Lobbrecht A. Volume change and light scattering during mechanical damage in polymethylmethacrylate toughened with core-shell rubber particles 1996;c:6409–22.

[27] Hourston DJ, Lane S, Zhang HX. Toughened thermoplastics: 2. Impact properties

and fracture mechanisms of rubber modified poly(butylene terephthalates). Polymer (Guildf) 1991;32:2215–20. doi:10.1016/0032-3861(91)90049-O.

[28] Stoeckel F, Konnerth J, Gindl-Altmutter W. Mechanical properties of adhesives for bonding wood-A review. Int J Adhes Adhes 2013;45:32–41. doi:10.1016/j.ijadhadh.2013.03.013.

[29] Garg, A. C.; Mai YW. Failure Mechanisms in Toughened Epoxy Resins A Review. Compos Sci Technol 1988;31:179–223.

[30] Hodgkin JH, Simon GP, Varley RJ. Thermoplastic toughening of epoxy resins: A critical review. Polym Adv Technol 1998;9:3–10.

[31] Mousavi SR, Amraei IA. Influence of nanosilica and methyl methacrylate-butadiene-styrene core-shell rubber particles on the physical-mechanical properties and cure kinetics of diglycidyl ether of bisphenol-A-based epoxy resin. High Perform Polym 2016;28:809–19. doi:10.1177/0954008315600228.

[32] Trimiño LF, Cronin DS. Evaluation of Numerical Methods to Model Structural Adhesive Response and Failure in Tension and Shear Loading. J Dyn Behav Mater 2016;2:122–37. doi:10.1007/s40870-016-0045-7.

[33] Avalle M, Peroni L, Peroni M, Scattina A. Bi-material joining for car body structures: Experimental and numerical analysis. Durab. Adhes. Joints, vol. 86, Politecnico Di Torino, Corso Duca Degli Abruzzi 24, 10129 Torino, Italy: Taylor and Francis Inc; 2010, p. 539–60.

[34] Yee AF, Pearson RA. Fractography and failure mechanisms of rubber modified epoxy resins. In: Roulin-Moloney A, editor. Fractography Fail. Mech. Polym. Compos., London: Elsevier applied science; 1989, p. 291.

[35] Sue HJ. Craze-like damage in a core-shell rubber-modified epoxy system. J Mater Sci 1992;27:3098–107. doi:10.1007/BF01154125.

[36] Sue H-J, Garcia-Meitin E, Orchard NA. Toughening of epoxies via craze-like damage. J Polym Sci Part B (Polymer Physics) 1993;31:595–608. doi:10.1002/polb.1993.090310511.

[37] Gent AN, Wang C. Fracture mechanics and cavitation in rubber-like solids. J Mater Sci 1991;26:3392–5. doi:10.1007/BF01124691.

[38] Bandyopadhyay S, Science D. Review of the Microscopic and Macroscopic Aspects of Fracture of Unmodified and Modified Epoxy Resins 1990;125:157–84.

[39] Gent AN. Hypothetical Mechanism of Crazing in Glassy Plastics 1970;5:925–32.

[40] Inglis CE. No Title. Trans Inst Nav Archit 1913;55:219.

[41] Paterson MS. Effect of Pressure on Young's Modulus and the Glass Transition in Rubbers. J Appl Phys 1964;35:176.

[42] Bin Ahmad Z, Ashby MF. Failure-mechanism maps for engineering polymers. J Mater Sci 1988;23:2037–50.

[43] Bordignon N, Piccolroaz A, Dal Corso F, Bigoni D. Strain Localization and Shear Band Propagation in Ductile Materials. Front Mater 2015;2:1–13. doi:10.3389/fmats.2015.00022.

[44] Bucknall CB, Kingdom U. Quantitative Approaches to Particle Cavitation , Shear Yielding , and Crazing in Rubber-Toughened Polymers 2006:1399–409. doi:10.1002/polb.

[45] Bigoni D, Dal Corso F. The unrestrainable growth of a shear band in a prestressed material. Proc R Soc A Math Phys Eng Sci 2008;464:2365–90. doi:10.1098/rspa.2008.0029.

[46] Rice JR. The Localization of Plastic Deformation. In: Koiter WT, editor. Int. Congr. Theor. Appl. Mech., Delf: 1976, p. 207–20.

[47] Lemaitre J. A course on damage mechanics. Berlin: Springer-Verlag; 1992.

[48] Lemaitre J, Dufailly J. Damage measurements. Eng Fract Mech 1987;28:643–61. doi:10.1016/0013-7944(87)90059-2.

[49] Wu G, Crocombe AD. Simplified finite element modelling of structural adhesive joints. Comput Struct 1996;61:385–91. doi:10.1016/0045-7949(96)00101-0.

[50] Shen W, Tang CY, Tsui CP, Peng LH. Effects of two damage mechanisms on effective elastic properties of particulate composites. Compos Sci Technol 2002;62:1397–406. doi:10.1016/S0266-3538(02)00085-4.

[51] Xin H, Brown HR, Naficy S, Spinks GM. Mechanical recoverability and damage process of ionic-covalent PAAm-alginate hybrid hydrogels. J Polym Sci Part B Polym Phys 2016;54:53–63. doi:10.1002/polb.23899.

[52] Shui G, Wang Y, Huang P, Qu J. Nonlinear ultrasonic evaluation of the fatigue damage of adhesive joints. NDT E Int 2015;70:9–15. doi:10.1016/j.ndteint.2014.11.002.

[53] Akbarzadeh P, Farhangdoost K. Fatigue life assessment of adhesive joints based on ratchetting strain evolution. Mech Adv Mater Struct 2016;23:681–8. doi:10.1080/15376494.2015.1029157.

[54] Mubashar A, Ashcroft IA, Crocombe AD. Modelling Damage and Failure in Adhesive Joints Using A Combined XFEM-Cohesive Element Methodology

2014:682–97. doi:10.1080/00218464.2013.826580.

[55] Cheng P, Gong X-J, Aivazzadeh S, Xiao X. Experimental observation of tensile behavior of patch repaired composites. Polym Test 2014;34:146–54. doi:10.1016/j.polymertesting.2014.01.007.

[56] Grave JHL, Echtermeyer AT. Strain fields in adhesively bonded patch repairs of damaged Metallic beams. Polym Test 2015;48:50–8. doi:10.1016/j.polymertesting.2015.09.013.

[57] de Freitas ST, Sinke J. Failure analysis of adhesively-bonded skin-to-stiffener joints: Metal-metal vs. composite-metal. Eng Fail Anal 2015;56:2–13. doi:10.1016/j.engfailanal.2015.05.023.

[58] Chiu WK, Galea SC, Koss LL, Rajic N. Damage detection in bonded repairs using piezoceramics. SMART Mater Struct 2000;9:466–75. doi:10.1088/0964-1726/9/4/309.

[59] Tsamasphyros GJ, Kanderakis GN, Marioli-Riga ZP. Thermal analysis by numerical methods of debonding effects near the crack tip under composite repairs. Appl Compos Mater 2003;10:149–58. doi:10.1023/A:1023945121389.

[60] Pavlopoulou S, Worden K, Soutis C. On the Structural Health Monitoring of Repaired Aerospace Structures. In: Chang, FK, editor. Struct. Heal. Monit. 2013, VOLS 1 2, 2013, p. 956+.

[61] Yavas D, Shang X, Hong W, Bastawros AF. Utilization of nanoindentation to examine bond line integrity in adhesively bonded composite structures. Int J Fract 2017;204:101–12. doi:10.1007/s10704-016-0165-z.

[62] Wu G, Qin Z, Zhang L, Yang K. Strain response analysis of adhesively bonded extended composite wind turbine blade suffering unsteady aerodynamic loads. Eng Fail Anal 2018;85:36–49. doi:10.1016/j.engfailanal.2017.12.009.

[63] de Ulzurrun ID, Lopez F, Herreros MA, Suarez JC. Tests of deck-to-hull adhesive Joints in GFRP boats. Eng Fail Anal 2007;14:310–20. doi:10.1016/j.engfailanal.2006.02.012.

[64] DEejong E, Duchatinier JG, Vannisselroij JJM. A Straightforward Ultrasonic Technique for the Inspection of Adhesively Bonded Connections and Sizing of Impact Damage in GRP Pipeines. INSIGHT 1994;36:683–5.

[65] Salamone S, Fasel T, Bartoli I, Srivastava A, di Scalea FL, Todd M. Health Monitoring Approach for Adhesively Bonded Joints. Mater Eval 2009;67:828–36.

[66] Ni X, Rizzo P. Use of Highly Nonlinear Solitary Waves in Nondestructive Testing. Mater Eval 2012;70:561–9.

[67] Severin F, Seviaryna I, Maeva E. Industrial Applications of Scanning Acoustic Microscopy. Mater Eval 2013;71:867–74.

[68] Crawford A, Droubi MG, Faisal NH. Analysis of Acoustic Emission Propagation in Metal-to-Metal Adhesively Bonded Joints. J Nondestruct Eval 2018;37. doi:10.1007/s10921-018-0488-y.

[69] 3M. 3M Scoth Weld, DP-460NS Technical data sheet n.d.

[70] Bowden PB. The yield behaviour of glassy polymers. In: Haward RN, editor. Phys. Glas. Polym., New York: Wiley; 1973, p. 279.

[71] Landini G. Image J, Auto Threshold 2017. https://imagej.net/Auto_Threshold (accessed April 9, 2016).

[72] Glasbey CA. An Analysis of Histogram-Based Threshold Algorithms. Graph Model Image Process 1993;55:532–7.

[73] Sezgin M. Survey over image thresholding techniques and quantitative performance evaluation 2004;13:146–65. doi:10.1117/1.1631316.

[74] Gonzales-Barron U, Butler F. A comparison of seven thresholding techniques with the k-means clustering algorithm for measurement of bread-crumb features by digital image analysis 2006;74:268–78. doi:10.1016/j.jfoodeng.2005.03.007.

[75] Surový P, Dinis C, Marušák R, Ribeiro NDA. Importance of automatic threshold for image segmentation for accurate measurement of fine roots of woody plants Význam automatického prahovania na obrazovú segmentáciu pre presné merania jemných koreňov drevín 2014;60:244–9.

[76] Sutton MA. Image correlation for shape, motion and deformation measurements basic concepts, theory and applications. New York: New York : Springer; 2009.

[77] VIC-2D 2009.

[78] ASTM. Standard,E11-04, 2010, Standard Test Method for Young's Modulus, Tangent modulus. and Chord modulus 2010. doi:10.1520/D3165.

[79] Low I, Mai Y. Micromechanisms of Crack Extension in Unmodified and Modified Epoxy Resins. Compos Sci Technol 1988;33:191–212.

[80] Cheung, M.F.; Plummer Jr H. lzod Impact Fracture Morphology of Rubber-toughened Polysulfone and Poly (Phenyene Sulfide) Blends. Polym Eng Sci 1996;36:15–22.

[81] Silicone Rubber mechanical properties n.d. http://www.azom.com/properties.aspx?ArticleID=920 (accessed August 11, 2016).

[82] Oxtoby DW. Principles of modern chemistry. Philadelphia: Saunders College Pub.; 1987.

[83] Shackelford JF. Introduction to materials science for engineers. 4th ed. Upper Saddle River, N.J.: Prentice Hall; 1996.

[84] Boyce MC, Parks DM, Argon AS. Large inelastic deformation of glassy polymers. part I: rate dependent constitutive model. Mech Mater 1988;7:15–33. doi:10.1016/0167-6636(88)90003-8.

[85] Qi HJ, Joyce K, Boyce MC. Durometer Hardness and the Stress-Strain Behavior of Elastomeric Materials. Rubber Chem Technol 2003;76:419–35. doi:10.5254/1.3547752.

[86] Mulliken AD, Boyce MC. Mechanics of the rate-dependent elastic–plastic deformation of glassy polymers from low to high strain rates. Int J Solids Struct 2006;43:1331–56. doi:10.1016/j.ijsolstr.2005.04.016.

[87] Lange FF. Interaction between overlaping paralell cracks; a photoelastic study. Int J Fract Mech 1968;4.

[88] Swain M V, Hagan JT. Some observations of overlaping interacting cracks. Eng Fract Mech 1978;10:299–304.

[89] Argon AS, Salama MM. Growth of crazes in glassy polymers. Philos Mag 1977;36:1217–34. doi:10.1080/14786437708239790.

[90] Kramer EJ. Craze Fibril Formation and Breakdown. Polym Eng Sci Sci 1984;24:761–9.

[91] Zhang H, Liu N, Ran X, Han C, Han L, Zhuang Y, et al. Toughening of Polylactide by Melt Blending with Methyl Methacrylate – Butadiene – Styrene Copolymer. J Appl Polym Sci 2012;125:E550–61. doi:10.1002/app.

[92] Mark 1934- JE. Physical properties of polymers handbook. 2nd ed. CN. New York: Springer; 2007.

Appendix

Section A-1: Viscoelastic effects in microhardness measurements

To clearly understand the potential for viscoelastic effects in DP-460NS, the undamaged material was subjected to micro-indentation. The micro-indentations were made using a Micro Vickers Hardness Machine (Leco MHD-200 model) and measurements were conducted using an opto-digital microscope (Keyence VHX-5000) at high magnification (1000x). Optical measurements of the indentations were conducted immediately after indentation and after a period of one week (Table A-1). The microhardness measurements were compare against the published microhardness for the material [37] (Figure A-1). The figure includes the microhardness average value (solid line) and the three standard deviation limits (dashed lines) of this figure. Statistical analysis was used to identify differences between the data sets mean average. The analysis was conducted using a T-test with 95% confidence (α=0.05). The T-test results (Table A-1) report that recorded differences in the mean value of the measurements were not statistically significant, therefore viscoelastic effects on this material are not expected.

1st measurement		2nd measurement	
Diagonal length [µm]	**HVN**	**Diagonal length [µm]**	**HVN**
165	136.23	165.1	136.06
189.3	103.50	182.5	111.35
127.4	228.50	160.9	143.26
134.8	204.10	170.9	126.98
159.2	146.33	170.3	127.88
168.4	130.78	163	139.59
176.7	118.78	189.7	103.06
190	102.74	201.6	91.25
Average	146.4		122.4
Std. dev	46.18		18.65

Table A-1: Microhardness indentations measurements

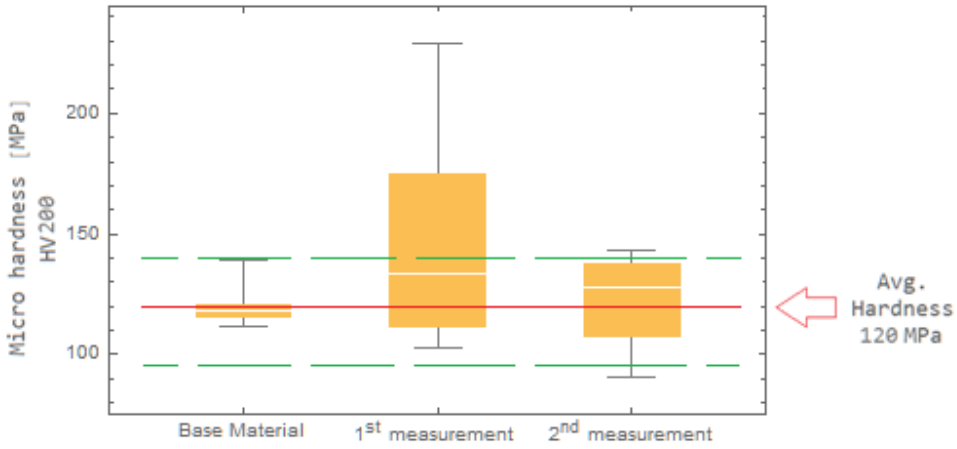

Figure A-2: Microhardness values

Set	T_{obs}	T_{crit}	P-Value
Base vs 1st	1.60	1.89	0.15
Base vs 2nd	0.33	1.86	0.75
1st vs 2nd	1.35	1.83	0.21

Table A-1: Statistical analysis

Section A2: Additional microscope observations: polished sample under load and post failure fracture plane

Additional observations were made at the surface of a polished sample under tension, at different levels of strain. Of notice was the detection of strain whitening at an embedded particle. The particle can be described as a circular black shell (~ 167 µm in diameter) with an interior white core (~66 µm in diameter). The color change started at the equator of the particle core and extended towards the shell with increases in strain. Finally, the strain whitening extended beyond the shell towards the surrounding area (Figure A-2), middle and far right) and the particle deformed into an ellipsoid for its final shape.

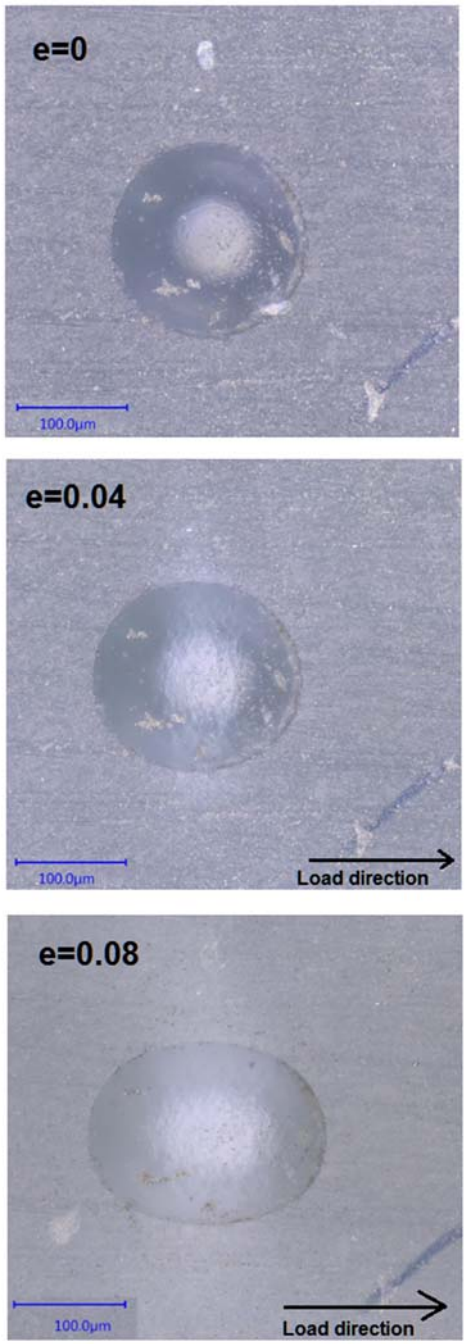

Figure A-2: Particle cavitation during increased axial loading

A fracture surface was studied using scanning electron microscopy (SEM). Although the fracture surface under SEM at various magnifications (Figure A-3) resembles the typical appearance of a toughened epoxy with thermoplastic toughening [31], the morphology of the fracture resembles that of furrows and steps. According to Low and Mei [79], this type of morphology is evidence of crack growth and arrest, and it is similar to those observed

in other toughened polymers [80]. No evidence of particle debonding was evident in the SEM observations.

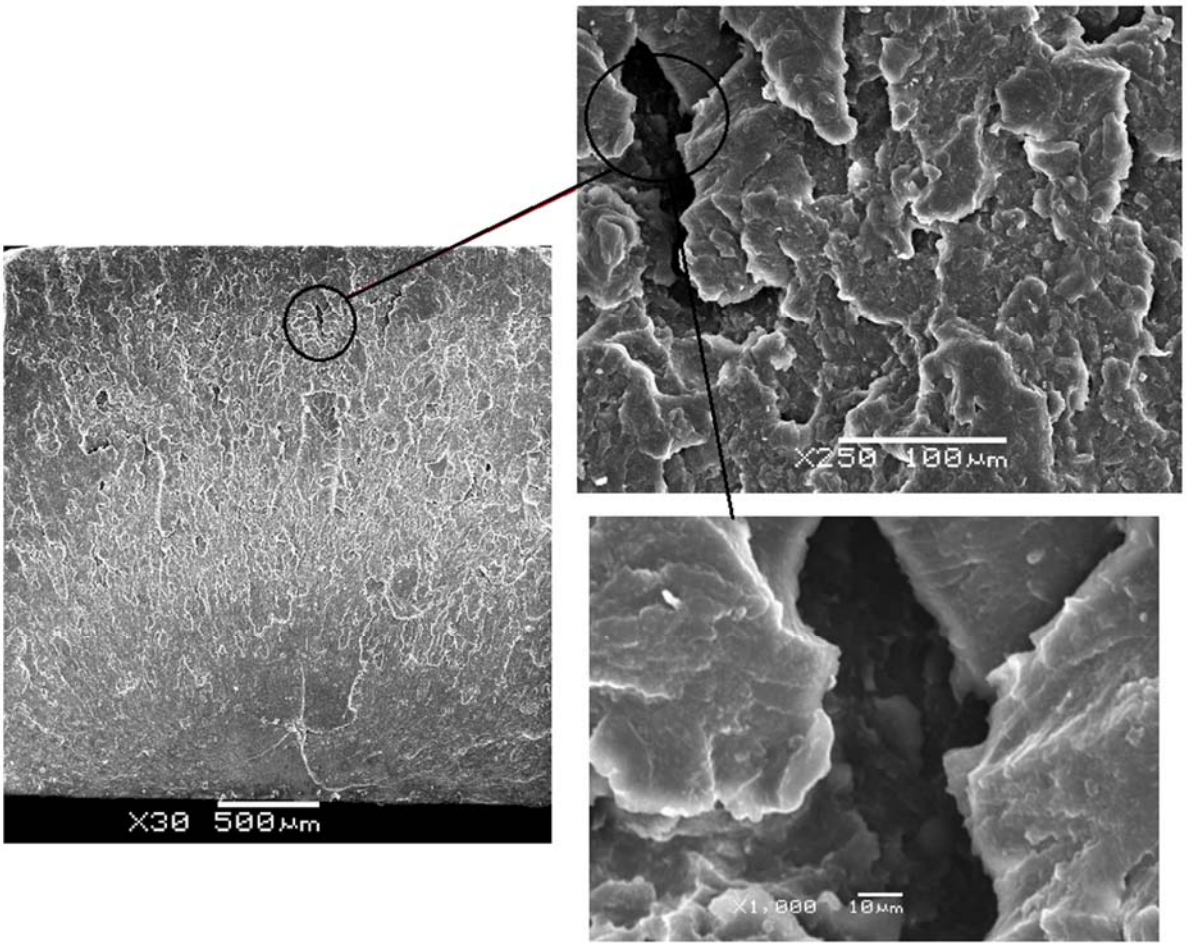

Figure A-3: Fracture plane on a sample tested to failure under quasi-static uniaxial tensile load

Section A3: Load-Unload measurements

The measurements of modulus of elasticity during load and unload are summarized in Tables A-3 to A-6. Each table corresponds to the tested displacements as per Table 3, and each table includes the coefficient of determination (r^2) and coefficient of variation (V_1).

Sample # and cycle	Load cycle			Unload cycle		
	E [GPa]	r^2	V_1 [%]	E [GPa]	r^2	V_1 [%]
A-LU-A2-cycle1	2.06	0.99	0.25	2.11	0.99	0.13
A-LU-A2-cycle2	1.93	0.99	0.17	1.98	0.99	0.13
A-LU-A2-cycle3	2.02	0.99	0.21	2.02	0.99	0.18
A-LU-A3-cycle 1	1.97	0.99	0.28	1,98	0.99	0.18
A-LU-A3-cycle 2	1.83	0.99	0.22	1.83	0.99	0.20
A-LU-A3-cycle 3	1.84	0.99	0.34	1.89	0.99	0.34
A-LU-A4-cycle 1	1.96	0.99	0.29	2.06	0.99	0.26
A-LU-A4-cycle 2	1.88	0.99	0.25	2.08	0.99	0.51
A-LU-A4-cycle 3	1.98	0.99	0.33	1.96	0.99	0.50

Table A-3: Modulus of elasticity measurements and calculation coefficients for applied strain of ~1.3% (Strain point A, Table 3)

Sample # and cycle	Load cycle			Unload cycle		
	E [GPa]	r^2	V_1 [%]	E [GPa]	r^2	V_1 [%]
A-LU-B2-cycle1	2.12	0.99	0.14	1.98	0.99	0.17
A-LU-B2-cycle2	1.91	0.99	0.13	1.91	0.99	0.19
A-LU-B2-cycle3	1.88	0.99	0.15	2.00	0.99	0.18
A-LU-B3-cycle 1	1.95	0.99	0.31	1.90	0.99	0.26
A-LU-B3-cycle 2	1.99	0.99	0.24	1.91	0.99	0.15
A-LU-B3-cycle 3	2.11	0.99	0.25	2.17	0.99	0.21
A-LU-B4-cycle 1	1.92	0.99	0.26	2.15	099	0.29
A-LU-B4-cycle 2	1.95	0.99	0.24	1.83	0.99	0.18
A-LU-B4-cycle 3	1.91	0.99	0.29	2.06	0.99	0.25

Table A-4: Modulus of elasticity measurements and calculation coefficients for applied strain of ~2% (Strain point B, Table 3)

Sample # and cycle	Load cycle			Unload cycle		
	E [GPa]	r^2	V_1 [%]	E [GPa]	r^2	V_1 [%]
A-LU-C4-cycle1	1.92	0.99	0.29	1.37	0.99	0.43
A-LU-C4-cycle2	1.73	0.99	0.73	1.39	0.98	0.77
A-LU-C4-cycle3	1.54	0.99	0.56	1.17	0.98	0.64
A-LU-C5-cycle 1	1.78	0.99	0.27	1.27	0.99	0.65
A-LU-C5-cycle 2	1.45	0.99	0.55	1.25	0.98	0.69
A-LU-C5-cycle 3	1.28	0.99	0.60	1.22	0.98	0.71
A-LU-C6-cycle 1	1.87	0.99	0.18	1.12	0.99	0.43
A-LU-C6-cycle 2	1.66	0.99	0.21	1.26	0.99	0.39
A-LU-C6-cycle 3	1.39	0.99	0.40	1.08	0.98	0.60

Table A-5: Modulus of elasticity measurements and calculation coefficients for applied strain of ~7% (Strain point C, Table 3)

Sample # and cycle	Load cycle			Unload cycle		
	E [GPa]	r^2	V_1 [%]	E [GPa]	r^2	V_1 [%]
A-LU-D1-cycle1	1.95	0.99	0.59	1.06	0.99	0.47
A-LU-D1-cycle2	1.58	0.98	1.09	1.31	0.98	0.67
A-LU-D1-cycle3	1.52	0.99	0.77	--	--	--
A-LU-D3-cycle 1	1.81	0.99	0.28	1.16	0.97	0.80
A-LU-D3-cycle 2	1.67	0.99	0.48	1.21	0.97	0.88
A-LU-D3-cycle 3	1.32	0.98	0.87	1.25	0.97	0.83
A-LU-D10-cycle 1	1.99	0.99	0.33	1.05	0.98	0.66
A-LU-D10-cycle 2	1.57	0.99	0.49	1.05	0.97	0.78
A-LU-D10-cycle 3	1.50	0.99		--	--	--

Table A-6: Modulus of elasticity measurements and calculation coefficients for applied strain of 8–10% (Strain point D, Table 3)